Structural and spectral properties of Galactic plane variable radio sources

Downloaded from: https://research.chalmers.se, 2026-10-07 18:45 UTC

Citation for the original published paper (version of record):
Yang, J., Chen, Y., Gurvits et al (2022). Structural and spectral properties of Galactic plane variable radio sources. Monthly Notices of the Royal Astronomical Society, 511(1): 280-294. http://dx.doi.org/10.1093/mnras/stab3804

N.B. When citing this work, cite the original published paper.

research.chalmers.se offers the possibility of retrieving research publications produced at Chalmers University of Technology. It covers all kind of research output: articles, dissertations, conference papers, reports etc. since 2004. research.chalmers.se is administrated and maintained by Chalmers Library

(article starts on next page)

Monthly Notices of the ROYAL ASTRONOMICAL SOCIETY

MNRAS **511,** 280–294 (2022) https://doi.org/10.1093/mnras/stab3804
Advance Access publication 2022 January 4

Structural and spectral properties of Galactic plane variable radio sources

Jun Yang [1,2★] Yongjun Chen,[3★] Leonid I. Gurvits [2,4] Zsolt Paragi [2] Aiyuan Yang [5] Xiaolong Yang [3] and Zhiqiang Shen[3]

[1]*Department of Space, Earth and Environment, Chalmers University of Technology, Onsala Space Observatory, SE-439 92 Onsala, Sweden*
[2]*Joint Institute for VLBI ERIC (JIVE), Oude Hoogeveensedijk 4, NL-7991 PD Dwingeloo, the Netherlands*
[3]*Shanghai Astronomical Observatory, Key Laboratory of Radio Astronomy, Chinese Academy of Sciences, 200030 Shanghai, China*
[4]*Department of Astrodynamics and Space Missions, Delft University of Technology, Kluyverweg 1, NL-2629 HS Delft, the Netherlands*
[5]*Max-Planck-Insitut für Radioastronomie, Auf dem Hügel 69, D-53121 Bonn, Germany*

Accepted 2021 December 22. Received 2021 December 2; in original form 2021 June 6

ABSTRACT

In the time domain, the radio sky in particular along the Galactic plane direction may vary significantly because of various energetic activities associated with stars, stellar, and supermassive black holes. Multi-epoch Very Large Array surveys of the Galactic plane at 5.0 GHz enabled the finding of a catalogue of 39 variable radio sources in the flux density range 1–70 mJy. To probe their radio structures and spectra, we observed 17 sources with the very-long-baseline interferometric (VLBI) imaging technique and collected additional multifrequency data from the literature. We detected all of the sources at 5 GHz with the Westerbork Synthesis Radio Telescope, but only G23.6644–0.0372 with the European VLBI Network (EVN). Together with its decadal variability and multifrequency radio spectrum, we interpret it as an extragalactic peaked-spectrum source with a size of $\lesssim$10 pc. The remaining sources were resolved out by the long baselines of the EVN because of either strong scatter broadening at the Galactic latitude $< 1^\circ$ or intrinsically very extended structures on centi-arcsec scales. According to their spectral and structural properties, we find that the sample has a diverse nature. We notice two young H II regions and spot a radio star and a candidate planetary nebula. The rest of the sources are very likely associated with radio active galactic nuclei (AGNs). Two of them also display arcsec-scale faint jet activity. The sample study indicates that AGNs are common place even among variable radio sources in the Galactic plane.

Key words: scattering – H II regions – Galaxy: general – radio continuum: galaxies – radio continuum: stars.

1 INTRODUCTION

Variable radio sources including slow transients represent rarely seen high-energy astrophysical processes. Their counterparts might be associated with active galactic nuclei (AGN), coronally active stars, accretion activity of the compact objects in binary systems (e.g. Pietka, Fender & Keane 2015; Mooley et al. 2016; Zhao, Morris & Goss 2020). Because they often have significant non-thermal radio emission, they are also important targets for very-long-baseline interferometry (VLBI) imaging observations to answer some fundamental questions. With the VLBI observations at centimetre wavelengths, we can probe their structures with a resolution of $\sim$1 mas and an astrometry precision of $\sim$10 μas (e.g. Reid & Honma 2014; Yang et al. 2016; Rioja & Dodson 2020). For nearby Galactic variable sources, the VLBI technique allows us to measure their distances and proper motions precisely (e.g. Atri et al. 2020; Ding et al. 2020), and reveals their structure changes on relatively short time-scales (e.g. Chomiuk et al. 2014).

Currently, multi-epoch radio sky surveys are becoming reachable and bringing us a more complete view of the dynamic radio sky. With the 36 dual-polarization beams, it took just 300 h for the full 36-antenna Australian Square Kilometre Array Pathfinder (ASKAP) telescope to finish the sky survey below Declination +40° (McConnell et al. 2020). The Rapid ASKAP Continuum Survey (RACS) has recently found 23 radio stars with significant circular polarization in the southern sky (Pritchard et al. 2021). The ASKAP Variables and Slow Transients (VAST) pilot survey has revealed a highly polarized transient point source (Wang et al. 2021) and 28 highly variable sources including several pulsars and radio stars (Murphy et al. 2021). The ongoing Karl G. Jansky Very Large Array Sky Survey (VLASS) at 2–4 GHz plans to have three epochs separated by 32 months (Lacy et al. 2020; Gordon et al. 2021). The VLASS at the first epoch has enabled the discoveries of a transient source consistent with a merger-triggered core collapse supernova (Dong et al. 2021), a decades-long extragalactic radio transient (Law et al. 2018), and a sample of quasars that brightened by a factor of 2–25 on decadal time-scales (Nyland et al. 2020). In the low-frequency regime 100–230 MHz, Ross et al. (2021) have identified several hundred sources with significant spectral variability over a year-long time-scale. According to the existing sky surveys, the fraction of variable radio sources and transients with a variability of $\gtrsim$30 per cent on time-scales of $\lesssim$10 yr and flux densities $>$0.1 mJy is about a few per cent (e.g. Mooley et al. 2016; Murphy et al. 2021).

★ E-mail: jun.yang@chalmers.se (JY); cyj@shao.ac.cn (YC)

© The Author(s) 2022.
Published by Oxford University Press on behalf of Royal Astronomical Society. This is an Open Access article distributed under the terms of the Creative Commons Attribution License (http://creativecommons.org/licenses/by/4.0/), which permits unrestricted reuse, distribution, and reproduction in any medium, provided the original work is properly cited.

Downloaded from https://academic.oup.com/mnras/article/511/1/280/6496041 by Chalmers Tekniska Hogskola user on 07 April 2022

The Galactic plane is of particular interest for various sky surveys to not only probe various Galactic objects (e.g. Brunthaler et al. 2021), but also reveal rarely seen variable sources. The VLA observations with an image sensitivity of ∼10 μJy beam^{-1} at 5.5 GHz show that the fraction of variable sources can reach ∼74 per cent at the Galactic Centre (Zhao et al. 2020). Using the historical VLA surveys (Becker et al. 1994; White, Becker & Helfand 2005; Purcell et al. 2013) of the Galactic plane (Galactic longitude: 20–45°, Galactic latitude: <1°) at three epochs (1990+, 2005, 2006), Becker et al. (2010) have compiled a catalogue of 39 variable radio sources. The multi-epoch VLA observations at 5 GHz show that these variable sources are not clearly resolved with a resolution of 1.5 arcsec in the pilot study (Becker et al. 2010) of Co-Ordinated Radio and Infrared Survey for High-mass star formation (CORNISH;[1] Hoare et al. 2012; Purcell et al. 2013) and more than 50 per cent of them varied by a factor of >2 over a time-scale of about 15 yr. These variable sources have a sky density of ∼1.6 per deg^2. In the flux density range 1–100 mJy, the sky density is twice higher than observed in extragalactic radio sources (de Vries et al. 2004). Because of the high sky density, a significant fraction of the catalogue are expected to be Galactic sources (Becker et al. 2010).

Becker et al. (2010) found that many variable sources (∼40 per cent) have flat or inverted radio spectra based on non-simultaneous measurements (Multi-Array Galactic Plane Imaging Survey or MAGPIS; Helfand et al. 2006) between 1.4 and 5 GHz. None of these sources has an optical counterpart (Becker et al. 2010). There are only 18 per cent of the sources coincident with mid-IR sources (Price et al. 2001; Benjamin et al. 2003; Carey et al. 2009) and 5 per cent of the sources associated with X-ray sources (Sugizaki et al. 2001; Hands et al. 2004). Several sources are likely to be associated with star-forming regions known from infrared and millimetre surveys (Price et al. 2001; Benjamin et al. 2003; Aguirre et al. 2011). For the entire catalogue, the absence of counterparts at other wavelengths might be due to intrinsically low flux densities instead of the heavily obscuration and absorption by the Galactic medium. The nature of the remaining 80 per cent variable sources was unknown. Among the known variable sources (e.g. Pietka et al. 2015), coronally active radio-emitting stars (e.g. RS Canum Venaticorum stars, Güdel 2002; Pritchard et al. 2021), radio pulsars including magnetars (e.g. Kaspi & Beloborodov 2017), or extragalactic transients (e.g. supernovae; Weiler et al. 2002) have been tentatively excluded by Becker et al. (2010) in view of their high variability, long life (∼15 yr) and relatively high flux density (0.5–70 mJy). The fact that these sources are variable and mainly detected in radio domain warrants their further investigation on the sub-arcsecond angular scales and the longer time-scales. To date, there are also some new sky surveys available, e.g. the RACS (Pritchard et al. 2021) and the VLASS (Lacy et al. 2020), for us to provide additional temporal and spectral information on the radio properties of these variable sources. These variable sources with the flat or inverted radio spectra are also candidate radio AGN (e.g. Orienti & Dallacasa 2020; O'Dea & Saikia 2021). Some radio AGN have long been known to vary intrinsically by factors of a few or more due to intrinsic effects (e.g. Hovatta et al. 2007; Nyland et al. 2020; Wołowska et al. 2021) and propagation effects at lower observing frequencies (e.g. Ross et al. 2021).

From the catalogue presented by Becker et al. (2010), we selected 17 sources for the European VLBI Network (EVN) observations at 5 GHz to explore their radio structures. These sources in Table 1 were selected mainly because they have nearby compact calibrators available (e.g. Immer et al. 2011) for us to run phase-referencing observations efficiently and reliably (e.g. Beasley & Conway 1995; Reid & Honma 2014). The sample also included the source G22.7194–0.1939, which was identified by Becker et al. (2010) as an object of special interest because its position is close to the centre of a supernova remnant.

Table 1. The 17 variable sources selected for the EVN observations at 5 GHz.

Source	Right ascension (J2000)	Declination (J2000)	Calibrator
(1)	(2)	(3)	(4)
G22.7194–0.1939	$18^h33^m21^s.033$	$-09°10'06''.43$	J1825–0737
G22.9116–0.2878	$18^h34^m02^s.837$	$-09°02'28''.03$	J1825–0737
G22.9743–0.3920	$18^h34^m32^s.343$	$-09°02'00''.69$	J1825–0737
G23.4186+0.0090	$18^h33^m55^s.619$	$-08°27'15''.92$	J1825–0737
G23.5585–0.3241	$18^h35^m23^s.014$	$-08°29'01''.42$	J1825–0737
G23.6644–0.0372	$18^h34^m33^s.050$	$-08°15'27''.10$	J1825–0737
G24.3367–0.1574	$18^h36^m13^s.893$	$-07°42'57''.64$	J1825–0737
G24.5343–0.1020	$18^h36^m23^s.987$	$-07°30'54''.26$	J1825–0737
G24.5405–0.1377	$18^h36^m32^s.343$	$-07°31'33''.52$	J1825–0737
G25.2048+0.1251	$18^h36^m49^s.735$	$-06°48'54''.63$	J1825–0737
G25.4920–0.3476	$18^h39^m03^s.094$	$-06°46'37''.38$	J1825–0737
G25.7156+0.0488	$18^h38^m02^s.785$	$-06°23'47''.29$	J1825–0737
G26.0526–0.2426	$18^h39^m42^s.626$	$-06°13'50''.28$	J1846–0651
G26.2818+0.2312	$18^h38^m26^s.372$	$-05°48'35''.17$	J1846–0651
G37.7347–0.1126	$19^h00^m36^s.987$	$+04°13'18''.60$	J1907+0127
G37.7596–0.1001	$19^h00^m37^s.037$	$+04°14'59''.08$	J1907+0127
G39.1105–0.0160	$19^h02^m47^s.984$	$+05°29'21''.52$	J1907+0127

Each column gives (1) source name, (2) right ascension, (3) declination, and (4) VLBI phase-referencing calibrator.

The paper is organized as follows. We describe our radio observations and data reduction in Section 2, and present the results observed with the EVN, the Westerbork Synthesis Radio Telescope (WSRT), the VLA, and the Very Long Baseline Array (VLBA) in Section 3. We discuss the nature of the only detected source G23.6644–0.0372, the effects of scatter broadening on the observed structures, and the classifications of these sources in Section 4. We give our conclusions in the last section. Through the paper, we define the spectral index $\alpha\alpha$ using the power-law spectrum $S(\nu)\propto\nu^{\alpha}$.

2 OBSERVATIONS AND DATA REDUCTION

2.1 The EVN experiments

With the EVN at 5.0 GHz, we observed the sample on 2010 December 15 and 16. We also carried out the follow-up observations of G23.6644–0.0372 on 2012 February 8 and September 17. The experiment configurations are summarized in Table 2. The participating stations were Effelsberg (EF), phased-up array (WB) of the WSRT, Jodrell Bank Mark II (JB2), Hartebeesthoek (HH), Onsala (ON), Noto (NT), Medicina (MC), Toruń (TR), Yebes (YS), and Cambridge (CM). The three experiments used a data rate of 1024 Mbps (16 MHz filters, 2 bit quantization, 16 sub-bands in dual polarization) in the *e*-VLBI mode (Szomoru 2008). The data were transferred from the European stations to Joint Institute for VLBI ERIC (European Research Infrastructure Consortium) via broadband internet connections and then correlated in the real-time mode by the EVN Mark IV data processor (Schilizzi et al. 2001) in 2010 and the EVN software correlator (SFXC; Keimpema et al. 2015) in 2012. The correlations were done with ordinary parameters for continuum experiments (1 or 2 s integration time, 16 or 32 points per sub-band).

[1] https://cornish.leeds.ac.uk/public/index.php

Downloaded from https://academic.oup.com/mnras/article/511/1/280/6496041 by Chalmers Tekniska Hogskola user on 07 April 2022

Table 2. The EVN observation configurations. The two-letter code for each VLBI station is explained in Section 2.

Project code	Frequency (GHz)	Bandwidth (MHz)	Starting UT	Duration (h)	Participating VLBI stations	Phase calibration	Sun distance (°)
EY014	5.004	128	2010 Dec 15, 13 h	11	EF, JB2, MC, ON, TR, WB, YS, HH, CM	Acceptable	21.1
EY017A	4.990	128	2012 Feb 08, 06 h	6	EF, JB2, MC, ON, TR, WB, YS	Successful	41.8
EY017B	4.990	128	2012 Sep 17, 15 h	7	EF, JB2, MC, ON, TR, WB, YS, NT	Successful	103.1

The VLBI observations were performed in the phase-referencing mode (e.g. Beasley & Conway 1995). The source positions (Becker et al. 2010) and the phase-referencing calibrators (Charlot et al. 2020) are listed in Table 1. The angular separations between each pair of sources are $\lesssim 4^\circ$. The cycle time was ∼4 min (∼60 s for calibrator, ∼120 s for target, ∼60 s for scan gaps. Each source was observed for 6–8 cycles. This gave us an actual image sensitivity of about 0.2 mJy beam^{-1}. We also observed the very bright (>10 Jy) calibrator 3C 454.3 as a fringe finder for a few short scans during each experiment.

During the observations of G23.6644–0.0372 on 2012 February 8 and September 17, we also observed a faint calibrator J1831–0756 as the secondary phase-referencing calibrator. The faint calibrator is just $0\overset{\circ}{.}9$ apart from the target and allows us to run another round of phase-referencing calibration to further remove residual phase errors.

We calibrated the visibility data with the National Radio Astronomy Observatory (NRAO) software package: AIPS (Astronomical Image Processing System; Greisen 2003). First, we inspected the visibility data and performed standard editing and flagging. Secondly, we did an a-priori amplitude calibration with the `antab` file, which saved antenna system temperatures and gain curves. Thirdly, we corrected the ionospheric dispersive delays via the task `TECOR`, the phase errors due to the antenna parallactic angle variations via the task `CLCOR`, and instrumental phase and delay offsets across sub-bands via the task `FRING`. Fourthly, we ran the fringe-fitting on the data combining all the sub-bands and the Stokes *RR* and *LL* correlations, and applied the solutions to all the sources. Finally, the instrumental bandpass shapes were corrected via the task `BPASS`. All AIPS tasks were run via the PARSELTONGUE interface (Kettenis et al. 2006).

Using the calibrated visibility data, we imaged all the sources in DIFMAP (Shepherd, Pearson & Taylor 1994). The phase-referencing calibrators were imaged through iterations of fitting the un-grided visibility data to some delta functions, i.e. point source models, and running self-calibration. During each iteration, new point-source models were manually added at the peak position in the residual map. Because this method ensures the applicability of the least-squares fitting for the whole iteration, it can allow us to gain a nearly random noise distribution in the residual map even in case of a poor (u, v) coverage and a heterogeneous VLBI network (e.g. Yang et al. 2020, 2021a). The bright calibrator J1825–0737 had an integrated flux density of 0.56 ± 0.03 Jy at 5.0 GHz in all three epochs. Fig. 1 shows its one-sided core-jet structure. The calibrator J1907+0127 displays a core-jet structure with a total flux density of 0.32 ± 0.02 Jy at 5 GHz in Fig. 2. The calibrator J1846–0651 shows a slightly resolved core-jet morphology with a total flux density of 0.101 ± 0.005 Jy at 5 GHz in Fig. 3. The three calibrator images are consistent with the exiting VLBI survey images (Charlot et al. 2020; Petrov 2021).

The faint nearby calibrator J1831–0756 had an integrated flux density of 44 ± 3 mJy. Fig. 4 displays its radio morphology, which is apparently resolved (size: ∼5.0 mas) and shows a very isotropic structure most likely because of the angular broadening by scattering

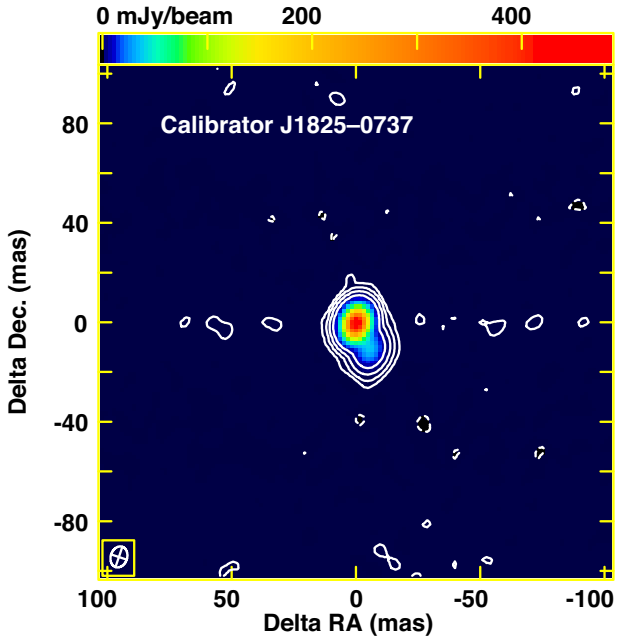

Figure 1. The jet structure of the bright phase-referencing calibrator J1825–0737 at 5 GHz on 2012 September 17. The map is made with natural weighting. The sizes of the beam FWHM are 8.6 × 6.6 mas at PA = $-18\overset{\circ}{.}5$. The map has a peak brightness of 484 mJy beam^{-1} and a noise level of σ = 0.028 mJy beam^{-1}. The contours represent the level of $3\sigma \times (-1, 1, 4, 16, 64)$. The image origin is at RA = $18^{\rm h}25^{\rm m}37\overset{\rm s}{.}60955$, Dec. = $-07^\circ37'30\overset{''}{.}0130$ (J2000).

in the Galactic ISM. The correlation amplitude on the longest baseline `ON--NT` (∼35 Mega-wavelengths) was ∼10 mJy.

With the input calibrator images, we re-ran the fringe-fitting and the amplitude and phase self-calibration in AIPS. All these amplitude and phase solutions were also transferred to the target data using a linear interpolation. The target sources were imaged without self-calibration. The observations on 2010 December 15 had a relatively small angular distance (about 21°) to the Sun, and suffered an unstable ionosphere. Thus, the fringe phase varied rapidly. This caused a relatively poor phase interpolation on the long baselines. However, on the short baselines, phase variation between neighbour scans was usually <180° and thus still acceptable for us to do an unambiguous phase interpolation.

2.2 The WSRT observations

We also processed the data obtained simultaneously with our VLBI run by the WSRT on 2010 December 15. The observations were performed with a linear array of ten 25-m telescopes deployed with a maximum baseline length of 2.7 km. The northern east–west array had an observing elevation of ≤30° and gave us a typical image resolution of ∼80 by ∼4 arcsec at 5 GHz with natural weighting for

Downloaded from https://academic.oup.com/mnras/article/511/1/280/6496041 by Chalmers Tekniska Hogskola user on 07 April 2022

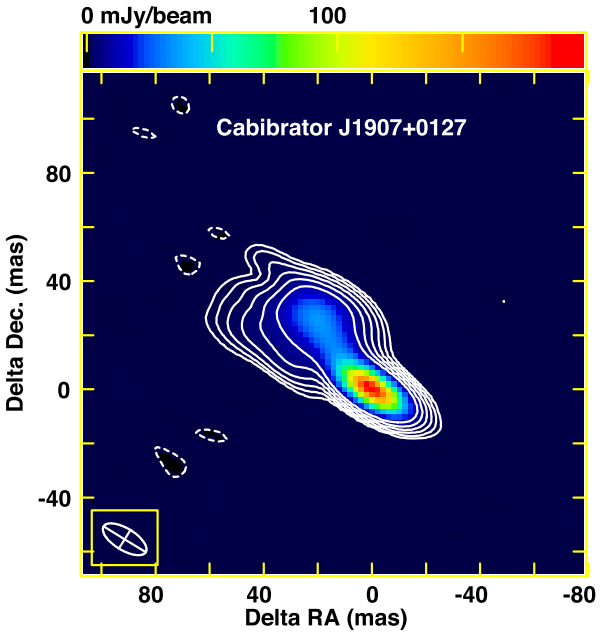

Figure 2. The core-jet structure of the phase-referencing calibrator J1907+0127 at 5 GHz. The map is made with natural weighting. The beam sizes are 18.3 × 8.05 mas at PA = −58.°5. The map has a peak brightness of 197 mJy beam^{-1} and a noise level of σ = 0.05 mJy beam^{-1}. The contours are at the levels 3σ × (−1, 1, 2, 4, 8, 16, 32, 64). The image origin is at RA = 19^{h}07^{m}11.^{s}99625, Dec. = +01°27′08.″9624 (J2000).

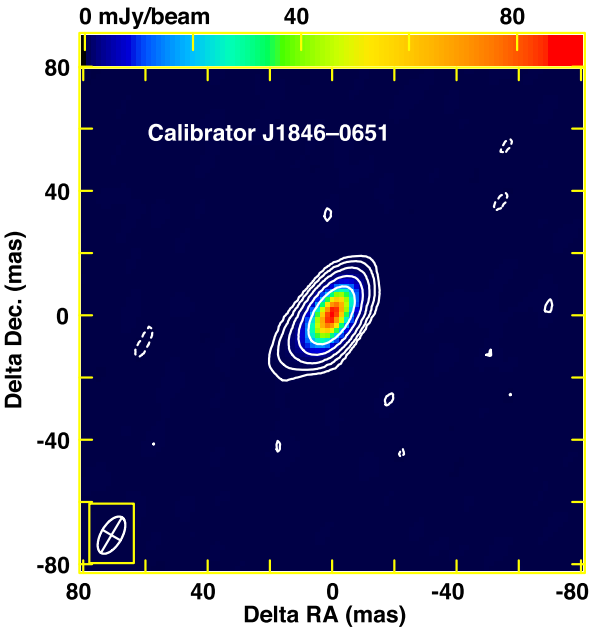

Figure 3. The slightly resolved jet structure of the phase-referencing calibrator J1846–0651. The map is made at 5 GHz with natural weighting. The sizes of the beam FWHM are 13.3 × 6.72 mas at PA = −30.°4. The map has a peak brightness of 91.6 mJy beam^{-1} and a noise level of σ = 0.024 mJy beam^{-1}. The contours are at the levels 3σ × (−1, 1, 4, 16, 64, 256). The image origin is at RA = 18^{h}46^{m}06.^{s}30027, Dec. = −06°51′27.″7460 (J2000).

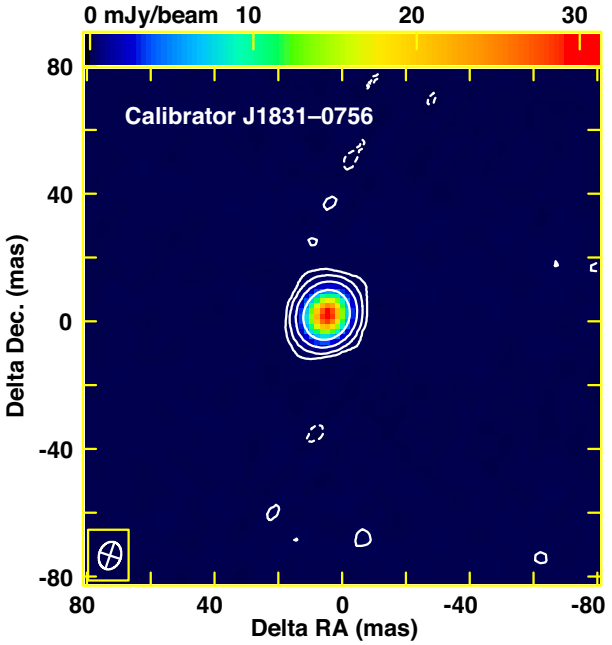

Figure 4. The isotropically resolved radio morphology of the nearby faint phase-referencing calibrator J1831–0756 (G23.540034+0.871604) at 5 GHz on 2012 September 17. The map is made with natural weighting. The sizes of the beam FWHM are 8.8 × 6.8 mas at PA = −18.°7. The map has a peak brightness of 31 mJy beam^{-1} and a noise level of σ = 0.027 mJy beam^{-1}. The contours are at the levels 3σ × (−1, 1, 4, 16, 64). The image origin is at RA = 18^{h}31^{m}03.^{s}67402, Dec. = −07°56′54.″1711 (J2000).

these low-Declination sources. During the observations, we observed 3C 48 as the primary flux density calibrator for two scans. After the labels of the linear polarization products were changed, the Stokes *XX* and *YY* correlation data were calibrated in the standard way recommended by the online AIPS cookbook[2] in Appendix A. During the data reduction, we used the model of Perley & Butler (2017) to calculate the flux density (5.4 Jy at 5 GHz) of 3C 48 and scaled the flux densities of the phase-referencing calibrators. In the (u, v) plane, we ran point-source model fitting to measure flux densities directly in DIFMAP. The output flux densities and the total uncertainties (including 5 per cent as systematic errors) are reported in Table 3.

2.3 Additional VLA and VLBA data

By chance, four sources were also observed with the VLA (project code 17A–070) C configuration at *X* band on 2017 June 2. These sources are listed in Table 4. Because they have rising spectra between 1.4 and 5 GHz (Yang et al. 2019), they were selected for the VLA observations to search for Galactic thermal sources. The VLA observations covered the band 8–12 GHz continuously to measure their spectra. The calibrator 3C 286 was observed as the primary flux density calibrator (Perley & Butler 2017). The sources J1851–0035 and J1832–1035 were observed as the phase-referencing calibrators. Each target source had an on-source time of ∼1 min. The data reduction was performed using the CASA (Common Astronomy Software Applications; McMullin et al. 2007) package. With the VLA pipeline,[3] the data were calibrated and processed.

[2]http://www.aips.nrao.edu/cook.html
[3]https://science.nrao.edu/facilities/vla/data-processing/pipeline

Downloaded from https://academic.oup.com/mnras/article/511/1/280/6496041 by Chalmers Tekniska Hogskola user on 07 April 2022

Table 3. Constraints on the angular sizes of the 17 Galactic plane sources.

No.	Source	S_{2011} (WSRT) (mJy)	S_{3MW} (EF--WB) (mJy)	θ_{FWHM} (EVN) (mas)	θ_{VLA5} (CORNISH) (arcsec)	V_f at 5 GHz (WSRT versus VLA)	Comments
(1)	(2)	(3)	(4)	(5)	(6)	(7)	(8)
1	G22.7194–0.1939	4.8 ± 0.4	≤1.8	≥35	1.50 ± 0.14	+0.15 ± 0.13	Candidate radio AGN
2	G22.9116–0.2878	15.6 ± 0.9	≤0.8	≥62	2.18 ± 0.10	−0.05 ± 0.08	Candidate radio AGN, 4.5 arcsec extension
3	G22.9743–0.3920	8.2 ± 0.7	≤1.5	≥47	1.50 ± 0.08	+0.13 ± 0.10	Candidate radio AGN
4	G23.4186+0.0090	4.2 ± 0.4	≤0.8	≥47	1.64 ± 0.12	−0.28 ± 0.12	Candidate radio AGN
5	G23.5585–0.3241	5.8 ± 0.5	≤2.1	≥36	1.90 ± 0.15	+0.06 ± 0.11	Candidate radio AGN
6	G23.6644–0.0372	23.8 ± 1.3	12.8	28	1.50 ± 0.04	−0.09 ± 0.09	VLBI detection, radio AGN
7	G24.3367–0.1574	6.9 ± 0.5	≤1.0	≥50	1.66 ± 0.11	+0.01 ± 0.11	Candidate radio AGN
8	G24.5343–0.1020	8.5 ± 0.7	≤0.9	≥54	1.50 ± 0.09	+0.61 ± 0.11	Radio star
9	G24.5405–0.1377	7.3 ± 0.7	≤0.9	≥52	1.50 ± 0.11	+0.47 ± 0.13	Candidate radio AGN
10	G25.2048+0.1251	6.5 ± 0.5	≤0.9	≥51	1.92 ± 0.19	+0.43 ± 0.12	Planetary nebula or radio AGN
11	G25.4920–0.3476	4.9 ± 0.5	≤0.8	≥49	1.50 ± 0.50	+0.84 ± 0.17	Candidate radio AGN
12	G25.7156+0.0488	16.5 ± 0.9	≤0.8	≥63	2.35 ± 0.03	+0.27 ± 0.08	H II region
13	G26.0526–0.2426	13.3 ± 0.8	≤2.5	≥47	1.50 ± 0.06	+0.05 ± 0.08	Candidate radio AGN
14	G26.2818+0.2312	19.6 ± 1.1	≤0.7	≥66	1.50 ± 0.04	+0.25 ± 0.08	Candidate radio AGN
15	G37.7347–0.1126	12.2 ± 0.8	≤0.8	≥60	1.78 ± 0.05	+0.00 ± 0.09	H II region
16	G37.7596–0.1001	13.0 ± 0.9	≤0.7	≥62	1.50 ± 0.05	+0.08 ± 0.09	Candidate radio AGN, 12.5 arcsec extension
17	G39.1105–0.0160	4.1 ± 0.5	≤1.1	≥41	2.24 ± 0.32	−0.02 ± 0.15	Candidate radio AGN

Each column gives (1) source number, (2) name, (3) total flux density measured by the simultaneous WSRT observations at 5 GHz on 2010 December 15, i.e. epoch 2011.0 (4) constraint on the correlation amplitude on the sensitive short baseline EF-WB (about three Mega-wavelengths), (5) constraint on the source angular size based on the correlation amplitudes, (6) angular size of the major axis reported by the 5-GHz VLA survey CORNISH (Hoare et al. 2012; Purcell et al. 2013) without de-convolution, (7) fractional variability between the 5-GHz flux densities observed by the WSRT at the epoch 2011.0 and the VLA at the epoch 2006.6 (Becker et al. 2010), (8) comments.

We notice that there were also VLBA observations of G23.6644–0.0372 (project code BH208M) at 8.4 GHz on 2015 August 10 (Pikky Atri, James Miller-Jones and Arash Bahramian, private communication). The observations had a recording data rate of 2048 Mbps (32 MHz filters, 2 bit quantization, 16 sub-bands in dual polarization). G23.6644–0.0372 was observed for 1 h in the phase-referencing mode with a cycle time of ∼3 min (∼30 s for J1825–0737, ∼120 s for G23.6644–0.0372, ∼30 s for two scan gaps). Following the VLBA continuum data calibration method recommended by the AIPS cookbook, we reduced the data.

3 RESULTS

3.1 WSRT and EVN imaging results

Among the 17 variable radio sources, only G23.6644–0.0372 was clearly detected in the EVN observations on 2010 December 15. Using the data on the shortest and most sensitive baseline EF--WB (distance 266 km), we made a dirty map and took the peak brightness as an upper limit on the average correlation amplitude for each source in Table 3. All the 17 sources were detected by the simultaneous low-resolution WSRT observations. Fig. 5 displays the 5-GHz flux densities measured by the WSRT at the epoch 2011.0 and the VLA at the epochs 2006.6 and 1990+ (Becker et al. 2010). Over the first two epochs 1990+ and 2006.6, 15 of 17 sources were greatly brightened (Becker et al. 2010). To search for significant variability between the later two epochs, we calculated the fractional variability V_f, which is defined as

$$V_f = 2\left(\frac{S_{2011} - S_{2006}}{S_{2011} + S_{2006}}\right). \quad (1)$$

The results are also listed in Table 3. Over 4.4 yr, one source (No. 8: G24.5343–0.1020) had a fractional variability of $>5\sigma$, and six sources (No. 4, 9–12, 14) had a fractional variability in the range 3–5σ.

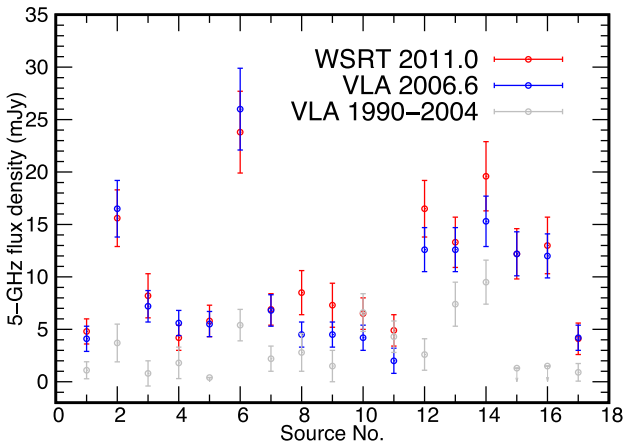

Figure 5. The flux densities observed at 5 GHz by the VLA at the epochs 1990+ and 2006.6 (Becker et al. 2010) and the WSRT at the epoch 2011.0. The error bars represent 3σ. The WSRT data are listed in Table 3. We notice that the non-detections of the sources No. 5, 15, and 16 at the early epoch were because of poor deconvolution (cf. Section 4.3).

For sources with a brightness distribution following a circular Gaussian function (e.g. Pearson 1995), we can describe its correlation amplitude $S(r)$ as

$$S(r) = S_0 \exp\left(\frac{-(\pi r \theta_{FWHM})^2}{4 \ln 2}\right), \quad (2)$$

where θ_{FWHM} is the source FWHM in radians, r is the (u, v) radius in wavelength, and S_0 is the correlation amplitude at $r = 0$, i.e. total flux density. Using the model 2, the measured WSRT flux density and the upper limit of the correlation amplitude on the baseline EF--WB

Downloaded from https://academic.oup.com/mnras/article/511/1/280/6496041 by Chalmers Tekniska Hogskola user on 07 April 2022

Table 4. The VLA X-band imaging results of four variable sources with the rising spectra at ≤5 GHz.

No.	Source	$S_{8.44}$ (mJy)	$S_{9.34}$ (mJy)	$S_{10.14}$ (mJy)	$S_{11.04}$ (mJy)	Beam (arcsec × arcsec)	α
(1)	(2)	(3)	(4)	(5)	(6)	(7)	(8)
4	G23.4186+0.0090	26.6 ± 1.3	26.3 ± 1.3	26.1 ± 1.3	25.6 ± 1.3	3.09 × 2.07	−0.13 ± 0.03
6	G23.6644–0.0372	30.4 ± 1.5	31.9 ± 1.6	32.7 ± 1.7	33.3 ± 1.7	3.06 × 2.06	+0.34 ± 0.04
8	G24.5343–0.1020	7.2 ± 0.4	8.0 ± 0.4	8.6 ± 0.5	8.8 ± 0.4	3.03 × 2.07	+0.73 ± 0.14
10	G25.2048+0.1251	7.7 ± 0.4	7.3 ± 0.4	7.2 ± 0.4	7.4 ± 0.4	2.98 × 2.08	−0.14 ± 0.14

Each column gives (1–2) source no. and name, (3–6) flux densities at 8.448, 9.344, 10.142, and 11.038 GHz, (7) beam size at 11.038 GHz, and (8) spectral index derived from the four simultaneous measurements.

at about three mega-wavelengths (Mλ), we derived a lower limit on the angular size for each source. These constraints are reported in Table 3. The minimum angular size among all sources in the observed sample is 28 mas. Moreover, we searched for their angular sizes in the CORNISH catalogue (Hoare et al. 2012; Purcell et al. 2013). The angular size of the major axis is reported in Table 3. Compared to the restoring beam size (1.5 arcsec), six sources are slightly resolved.

These sources have been also observed at 2–4 GHz in the ongoing survey VLASS (Lacy et al. 2020). The survey has a resolution of 2.5 arcsec and a sensitivity of 0.12 mJy beam^{-1} per epoch. Using the image cutout web service[4] provided by the Canadian Initiative for Radio Astronomy Data Analysis (CIRADA), we downloaded their total intensity images that had the more accurate flux density calibration at the later epochs 1.2 and 2.1. During the multi-epoch VLA observations between 2019 March 10 and 2020 August 12, all the 17 sources were clearly detected. We used the AIPS task JMFIT to determine their integrated flux densities. The flux densities at 3.00 GHz are presented in Table 5. We also used 5 per cent of the total flux density as the systematic errors.

In the continuum survey RACS at 887.5 MHz (McConnell et al. 2020), 10 sources from our sample were clearly detected. We also list their flux densities in Table 5. If the source is not detected, we only give a 5σ (the survey median value $\sigma = 0.25$ mJy beam^{-1}) upper limit on its total flux density. Using the surveys RACS and VLASS with a time interval of about 1 yr, we also derived a non-simultaneous spectral index between 887.5 MHz and 3.0 GHz for each source in Table 5. Because a systematic error of ∼5 per cent is included in the two surveys, the spectral index estimate may be affected significantly by a fractional variability of >15 per cent.

These Galactic plane sources are also observed by The HI/OH/Recombination line survey of the inner Milky Way (THOR; Bihr et al. 2016; Wang et al. 2018, 2020) in 2013. The observations with the VLA at 1–2 GHz used eight 128-MHz sub-bands with the centre frequencies from 1.052 to 1.948 MHz, and gained image resolutions 10–40 arcsec. The continuum source catalogue provides simultaneously flux density measurements and spectral indices. In the catalogue, we searched for our target sources with a radius of 5 arcsec and found 13 sources. We also checked their online images to further verify these detections. Their flux densities at 1.05, 1.44, and 1.95 GHz; and spectral indices are reported in Table 5.

3.2 The multi-epoch EVN imaging results of G23.6644–0.0372

The left-hand panel in Fig. 6 shows the imaging results for G23.6644–0.0372. The Stokes *I* image was made using the data on the short baselines ≤10 Mλ and natural weighting. The source does not look clearly resolved in the image plane. However, the correlation amplitude varies significantly from ∼15 to ∼5 mJy on the shortest baseline EF--WB, indicating that the source is significantly resolved (e.g. Pearson 1995). The correlation amplitude variation is also displayed in the right-hand panel of Fig. 6. On the other baselines, fringes are not clearly seen. Without the baseline EF--WB, G23.6644–0.0372 shows a peak brightness of 0.18 mJy beam^{-1}, which is slightly below the general 5σ detection limit in the dirty map with natural weighting. This indicates that the source has a very low surface brightness and is overresolved (e.g. Pearson 1995). We tried to fit the short-baseline visibility data to both circular and elliptical Gaussian models in DIFMAP. The visibility data and the models on the baseline EF--WB in the first sub-band are shown in Fig. 7. Compared to the circular Gaussian model, the elliptical Gaussian model gives a 2 per cent smaller reduced χ^2 and fit the long baseline data (cf. Fig. 6) of EF--WB more reasonably. In view of the more accurate fitting, we only report the results of the elliptical Gaussian model in Table 6. The uncertainties associated with the best-fitting parameters are the formal errors at the reduced $\chi^2_{\rm red} = 1$. The systematic uncertainty for the integrated flux density is ∼1.3 mJy (∼5 per cent). We excluded the long baseline data at the radius >10 Mλ in the model fitting.

Over the three epochs of EVN observations covering about 2 yr, G23.6644–0.0372 had no detectable proper motion. Fig. 8 presents the measured positions and sizes. The source centroid has a large scatter along the major extension direction. This mainly results from some systematic residual phase errors of the phase-referencing calibrations (Reid & Honma 2014; Rioja & Dodson 2020). Our target had small angular distances from the Sun (cf. Table 2) in the first two epochs. Because of solar activity, the interplanetary plasma and the Earth's ionosphere varied significantly from epoch to epoch. These observations also had relatively low observing elevations (15–31° at EF and WB). The useful (u, v) coverage was limited to a few short baselines owning to the heavily resolved source structure. Moreover, the sensitive baseline EF--WB gave some strong sidelobes in the dirty map. Thus, the EVN observations failed to achieve a typical astrometric precision of <1 mas (e.g. Yang et al. 2016; Rioja & Dodson 2020). The average J2000 centroid position for G23.6644–0.0372 is RA = $18^{\rm h}34^{\rm m}33\overset{\rm s}{.}0457$, Dec. = $-08^\circ15'27\overset{''}{.}142$. Assuming a stationary centroid, we estimate the standard deviations: $\sigma = 2.2$ mas in RA, $\sigma = 2.4$ mas in Dec. The source structure shows a consistent extension along the direction $\theta_{\rm pa} = 39\overset{\circ}{.}4 \pm 2\overset{\circ}{.}7$. The average ellipsoid axes are $\theta_{\rm maj} = 43.4 \pm 0.7$ mas and $\theta_{\rm min} = 28.7 \pm 1.3$ mas.

The brightness temperature $T_{\rm b}$ is estimated (e.g. Condon et al. 1982) as

$$T_{\rm b} = 1.22 \times 10^9 \frac{S_{\rm int}}{\nu^2_{\rm obs}\theta_{\rm maj}\theta_{\rm min}}(1+z), \quad (3)$$

where $S_{\rm int}$ is the integrated flux density in mJy, $\nu_{\rm obs}$ is the observing frequency in GHz, z is the redshift and unknown, $\theta_{\rm maj}$ and $\theta_{\rm min}$ are the

[4] http://cutouts.cirada.ca/

Downloaded from https://academic.oup.com/mnras/article/511/1/280/6496041 by Chalmers Tekniska Hogskola user on 07 April 2022

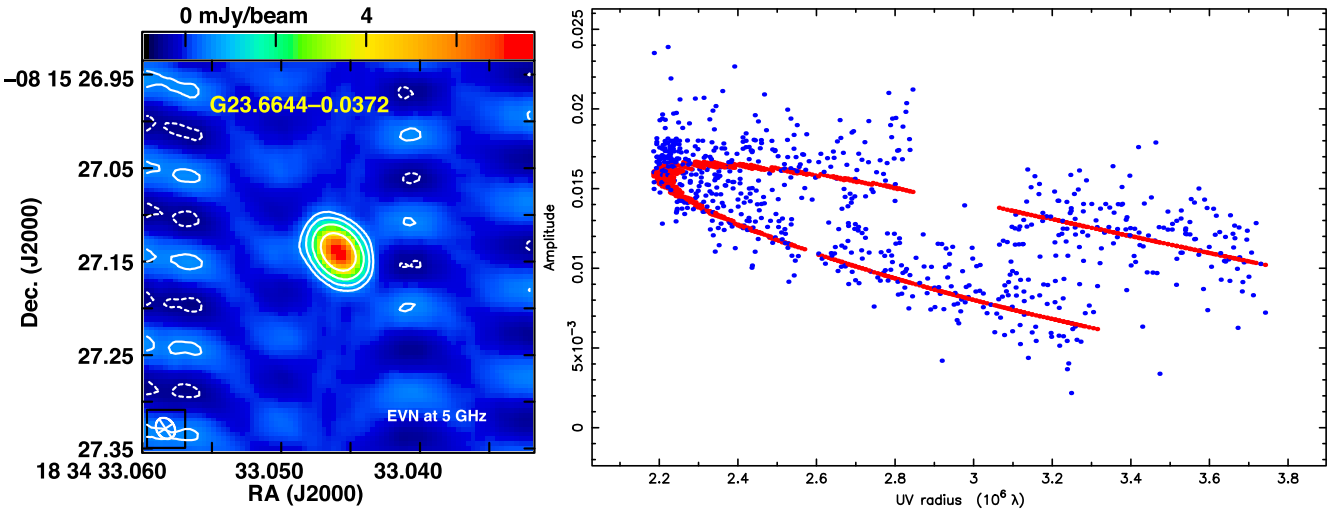

Figure 6. The Stokes *I* map and the best-fitting model of the variable radio source G23.6644–0.0372. Left-hand panel: the intensity map at 5 GHz on 2012 September 17. The image has a noise level of $\sigma = 0.2$ mJy beam^{-1} and a peak brightness of 7.6 mJy beam^{-1}. The sizes of the beam are FWHM = 24 × 19 mas at PA = 33°.4. The contours represent the levels $2.5\sigma \times (-1, 1, 2, 4, 8)$. Right-hand panel: The correlation amplitude in Jy versus the (u, v) radius in Mega-wavelengths for the source G23.6644–0.0372 on the shortest baseline of EF--WB. The red dots represent the best-fitting elliptical Gaussian model used in the image. The blue dots show the visibility data.

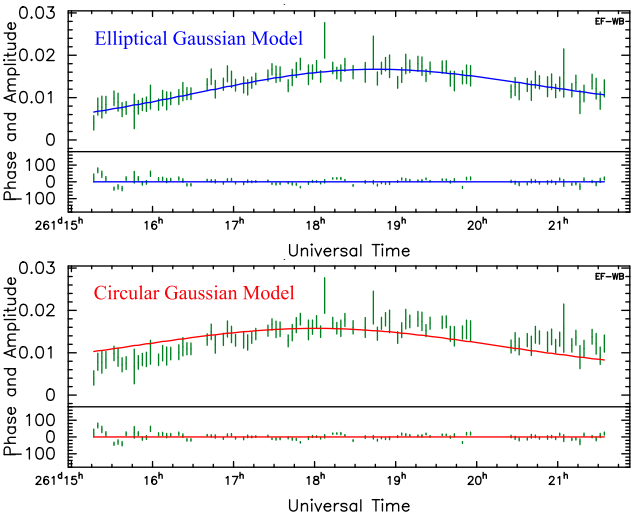

Figure 7. The best-fitting circular and elliptical Gaussian models and the visibility data on the short baseline EF--WB in the first sub-band.

FWHM in mas. The average brightness temperature over the three epochs will be $(1.1 \pm 0.1) \times 10^6(1 + z)$ K.

3.3 Imaging results of the additional VLA and VLBA data

The broad-band VLA observations gave us a sensitivity of ∼0.1 mJy beam^{-1} and a resolution up to ∼3 by ∼2 arcsec. All the four sources are clearly detected. The simultaneous multifrequency flux density measurements are listed in Table 4. The flux densities were measured from the sub-band data of 1 GHz bandwidth. Since some channels with poor data were flagged out, each sub-band had a valid bandwidth of about 900 MHz. For each source, we also tried to estimate the angular size by model-fitting a circular Gaussian model with the CASA task UVMODELFIT. However, the deconvolved angular sizes (≤57 mas) are much smaller than the beam sizes and there are no significant differences between the total flux densities and the image peak values, indicating that these sources are unresolved. From the four simultaneous flux density measurements, the spectra index is also estimated and listed in Table 4.

G23.6644–0.0372 also displays a significant resolved structure at 8.4 GHz. In Fig. 9, its correlation amplitude declines significantly on the long baselines. Using an elliptical Gaussian model and the calibrated visibility data from the four short-baseline stations (Los Alamos, Pie Town, Owens Valley, and Kitt Peak), we derived $S_{\rm int} = 27.7 \pm 1.8$ mJy (including an empirical systematic error of 5 per cent), $\theta_{\rm maj} = 15.8 \pm 0.8$ mas, $\theta_{\rm min} = 10.1 \pm 1.4$ mas, and $\theta_{\rm pa} = 38.0 \pm 3.4$ deg. The predicted values of the model are also plotted as the red points in Fig. 9. The total flux density is consistent with that observed by the VLA (cf. Table 4).

4 DISCUSSION

Based on the above inputs and the available multiwavelength data in literature, we probe the natures of the 17 sources. First, the only VLBI-detected source G23.6644–0.0372 is studied in details. Secondly, the general structural properties of the sample and the contributions of the scatter broadening are discussed. Finally, the possible nature and the spectral classification for each source are probed.

4.1 G23.6644–0.0372: a broadened image of a compact source

Diffuse, turbulent, and ionized gas in the Galactic interstellar medium (ISM) scatters radio waves and might cause significant temporal and angular broadening in particular at low observing frequencies and close to the Galactic plane (e.g. Fey, Spangler & Cordes 1991; Cordes et al. 1991; Cordes & Lazio 2002). Radio observations of intrinsically compact sources along the Galactic plane can also offer some potential for probing the medium. The spatial power spectrum of the interstellar density fluctuations is a power law,

$$P_{\delta n_e} = C_n^2 q^{-\epsilon}, \quad (4)$$

Downloaded from https://academic.oup.com/mnras/article/511/1/280/6496041 by Chalmers Tekniska Hogskola user on 07 April 2022

Table 5. Total flux densities of the 17 variable sources.

No.	Source	$S_{0.88}$ (mJy)	$S_{1.06}$ (mJy)	$S_{1.44}$ (mJy)	$S_{1.95}$ (mJy)	$S_{3.00}$ (mJy)	$\alpha_{1.0}^{2.0}$	$\alpha_{0.9}^{3.0}$
(1)	(2)	(3)	(4)	(5)	(6)	(7)	(8)	(9)
1	G22.7194–0.1939	16.2 ± 1.6	18.0 ± 3.1	10.7 ± 1.6	7.2 ± 1.3	6.4 ± 0.7	−1.68 ± 0.36	−0.77 ± 0.12
2	G22.9116–0.2878	72.1 ± 5.5	55.6 ± 2.8	47.4 ± 2.0	32.2 ± 1.7	28.8 ± 1.3	−0.96 ± 0.09	−0.75 ± 0.07
3	G22.9743–0.3920	13.1 ± 1.4	10.1 ± 5.1	9.5 ± 2.8	5.7 ± 2.0	10.3 ± 0.9	−1.31 ± 2.71	−0.20 ± 0.11
4	G23.4186+0.0090	≤1.3				4.9 ± 0.6		≥1.1
5	G23.5585–0.3241	15.6 ± 1.6	14.5 ± 2.4	11.2 ± 1.5		8.1 ± 0.8	−0.59 ± 0.45	−0.54 ± 0.12
6	G23.6644–0.0372	≤1.3				13.5 ± 0.9		≥1.9
7	G24.3367–0.1574	23.9 ± 2.2	25.5 ± 0.3	18.9 ± 2.1		12.5 ± 0.9	−0.54 ± 0.26	−0.53 ± 0.10
8	G24.5343–0.1020*	≤1.3				4.8 ± 0.7		≥1.10
9	G24.5405–0.1377	≤1.3	2.2 ± 3.4	4.9 ± 2.1	3.4 ± 1.6	6.8 ± 0.8		≥1.40
10	G25.2048+0.1251	≤1.3	4.4 ± 2.2	4.8 ± 1.7	4.7 ± 1.2	6.9 ± 0.7	+0.38 ± 1.06	≥1.40
11	G25.4920–0.3476	13.8 ± 1.4	7.3 ± 2.1	8.1 ± 1.6	2.3 ± 1.9	6.2 ± 0.7	+0.36 ± 1.08	−0.65 ± 0.13
12	G25.7156+0.0488*	≤1.3	12.2 ± 4.2	15.3 ± 2.4		21.4 ± 1.4	+0.58 ± 0.54	≥2.3
13	G26.0526–0.2426	24.7 ± 2.2	22.1 ± 1.4	20.1 ± 1.2		15.5 ± 1.0	−0.38 ± 0.15	−0.38 ± 0.09
14	G26.2818+0.2312	25.8 ± 2.3	25.9 ± 1.4	25.7 ± 1.0		18.8 ± 1.0	+0.00 ± 0.13	−0.26 ± 0.09
15	G37.7347–0.1126*	≤1.3	15.7 ± 0.4	13.3 ± 2.1	11.3 ± 1.5	13.5 ± 1.0	−0.27 ± 0.38	≥1.9
16	G37.7596–0.1001	31.6 ± 2.7				11.5 ± 1.0		−0.83 ± 0.10
17	G39.1105–0.0160	14.3 ± 1.5	12.4 ± 1.2	12.1 ± 1.0	12.8 ± 1.5	8.6 ± 0.8	−0.15 ± 0.19	−0.42 ± 0.11

Columns give (1) source number, (2) name (the superscript *: Galactic star or H II region), (3) flux density from the ASKAP survey RACS at 887.5 MHz between 2019 and 2020 (McConnell et al. 2020), (4–6) flux densities from the VLA survey THOR at 1.06, 1.44, and 1.95 GHz in 2013 (Bihr et al. 2016), (7) flux density from the survey VLASS between 2019 March 10 and 2020 August 12 (Lacy et al. 2020), (8) simultaneous spectral index measured by the survey THOR, and (9) non-simultaneous spectral index between 0.9 and 3.0 GHz.

Table 6. Summary of the elliptical Gaussian model fitting results and map parameters of G23.6644–0.0372.

MJD	$S_{\rm int}$ (mJy)	ΔRA (mas)	ΔDec (mas)	$\theta_{\rm maj}$ (mas)	$\theta_{\rm min}$ (mas)	$\theta_{\rm pa}$ (°)	$S_{\rm pk}$ (mJy beam^{-1})	$\phi_{\rm maj}$ (mas)	$\phi_{\rm min}$ (mas)	$\phi_{\rm pa}$ (°)
(1)	(2)	(3)	(4)	(5)	(6)	(7)	(8)	(9)	(10)	(11)
55546.5	24.5 ± 2.0	−63.0 ± 0.5	−42.3 ± 0.3	48.9 ± 1.6	28.6 ± 3.0	+55.4 ± 5.5	5.5 ± 0.9	22.6	18.0	35.1
55965.4	29.2 ± 2.0	−65.3 ± 0.1	−44.4 ± 0.1	41.2 ± 1.2	29.1 ± 1.9	+24.0 ± 4.7	10.4 ± 0.4	27.0	25.0	10.1
56187.8	26.4 ± 1.6	−61.1 ± 0.1	−39.6 ± 0.1	39.9 ± 0.6	28.6 ± 0.9	+38.9 ± 3.5	7.6 ± 0.2	24.0	19.0	33.4

Columns give (1) MJD, (2) total flux density, (3–4) relative offsets in Right Ascension and Declination with respect to the VLA position (RA = $18^{\rm h}34^{\rm m}33\overset{\rm s}{.}05$, Dec = $-08°15'27\overset{''}{.}1$, J2000), (5–6) sizes of major and minor axes of the elliptical Gaussian model, (7) position angle, (8) map peak brightness and statistical rms, (9–11) sizes of major and minor axes of the synthesized beam, and position angle of the major axis. The errors in columns (2–7) are formal errors from the model fitting in DIFMAP at the reduced $\chi_{\rm red} = 1$.

where C_n^2 is the spectral coefficient, q is the wavenumber with q_0 and q_1 corresponding to the outer and inner scales of the turbulence, respectively. The density spectral index ϵ is empirically determined to be ∼11/3 (e.g. Cordes et al. 1991). The scattering measure (SM) representing the line-of-sight integral of the power spectrum normalization constant can be expressed as,

$$\mathrm{SM} = \int_0^D C_n^2(s)\mathrm{d}s, \tag{5}$$

where D is the path-length through the scattering medium. Because of angular broadening, the observed angular size $\theta_{\rm obs}$ follows $\theta_{\rm obs}^2 = \theta_{\rm int}^2 + \theta_{\rm scat}^2$, where $\theta_{\rm int}$ is the intrinsic source size and $\theta_{\rm scat}$ is the contribution from the scatter broadening. In case of an intrinsically compact source, i.e. $\theta_{\rm int} \ll \theta_{\rm scat}$, one can get $\theta_{\rm obs} = \theta_{\rm scat}$. Under the assumption of a uniform medium, the measurement $\theta_{\rm scat}$ can allow us to provide an estimate for SM via the relation (Cordes & Lazio 2002, 2003)

$$\mathrm{SM} = \left(\frac{\theta_{\rm scat}}{\theta_0}\right)^{5/3} \nu^{11/3}, \tag{6}$$

where SM is in kpc m$^{-20/3}$, ν is in GHz, $\theta_0 = 128$ mas for extragalactic sources and $\theta_0 = 71$ mas for Galactic sources. The equation (6) predicts a strong dependence of $\theta_{\rm scat} \propto \nu^{-11/5}$.

The pulsar observations can also measure SM (Cordes & Lazio 2002, 2003)

$$\mathrm{SM} = 292 \left(\frac{\tau_{\rm d}}{D}\right)^{5/6} \nu^{11/3}, \tag{7}$$

where $\tau_{\rm d}$ is the time delay because of temporal broadening in s and D is the distance to the pulsar. This method only applies to pulsars because it requires very narrow pulses.

G23.6644–0.0372 can be explained as a compact radio AGN seen in the presence of strong scattering when its radio emission propagates through the turbulent ISM of the Galactic plane. Fig. 10 plot the sizes of the major and minor axes at 5.0 and 8.4 GHz. It is clearly seen that the observed sizes show a strong frequency dependence. The dependence can be written as

$$\theta_{\rm maj} = \theta_{\rm obs1} \left(\frac{\nu}{\nu_{\rm obs}}\right)^{-1.93\pm0.10}, \tag{8}$$

$$\theta_{\rm min} = \theta_{\rm obs2} \left(\frac{\nu}{\nu_{\rm obs}}\right)^{-2.00\pm0.28}, \tag{9}$$

where $\theta_{\rm obs1}$ and $\theta_{\rm obs2}$ represent the observed angular sizes of the major and minor axes at the frequency $\nu_{\rm obs}$. The two power-law relations are consistent with the expectation of the scatter broadening. The derived SM is in the ranges of 30–60 kpc m$^{-20/3}$

Downloaded from https://academic.oup.com/mnras/article/511/1/280/6496041 by Chalmers Tekniska Hogskola user on 07 April 2022

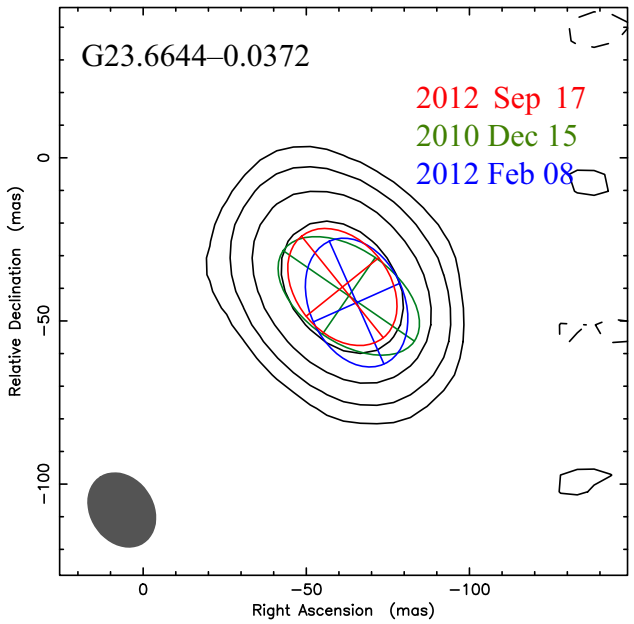

Figure 8. The multi-epoch positions and sizes of the variable radio source G23.6644–0.0372. The contour image in Fig. 6 is also overplotted here. The data in details are reported in Table 6.

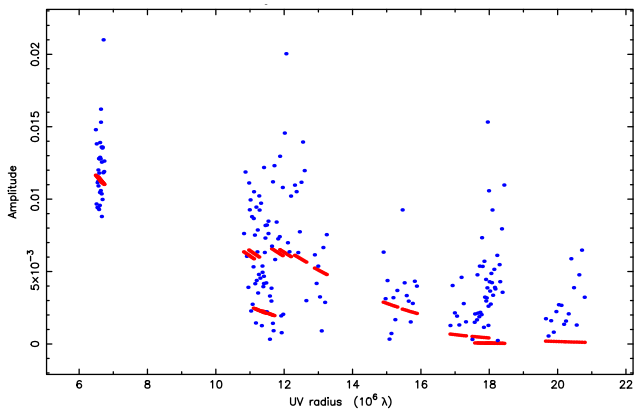

Figure 9. Plot of the 8.4-GHz correlation amplitude in Jy versus the (u, v) radius in Mλ. The blue points represent the visibility data observed by the VLBA and averaged with an interval of 15 min. The red points display the best-fitting elliptical Gaussian model. The amplitude drop on the long baselines indicates that G23.6644–0.0372 is significantly resolved.

for an extragalactic source and 80–160 kpc m$^{-20/3}$ for a galactic source. The anisotropic structure roughly along the Galactic plane direction can be produced by the source itself, the magnetic field in the scattering medium (e.g. Trotter, Moran & Rodríguez 1998; Kounkel et al. 2018) or both. To date, there are many similar objects reported in the literature (e.g. Fey et al. 1991; Pushkarev & Kovalev 2015). The most strongly broadened object is NGC 6334B (Moran et al. 1990), which has apparent angular sizes 0.34 by 0.27 arcsec at 4.9 GHz because of anisotropic radio-wave scattering (Trotter et al. 1998). Sagittarius A* (Sgr A*) is another case studied intensively by multiwavelength VLBI observations (e.g. Shen et al. 2005; Johnson et al. 2018). Its two-dimensional scattering structure can be described as $\theta_{\rm maj} = (1.39 \pm 0.02)\lambda^2$ mas by $\theta_{\rm min} = (0.69 \pm 0.06)\lambda^2$ mas with a position angle of ∼80° (Shen et al. 2005), where λ is in cm. The source J053424.63–052838.5 at the edge of the Orion nebula has a

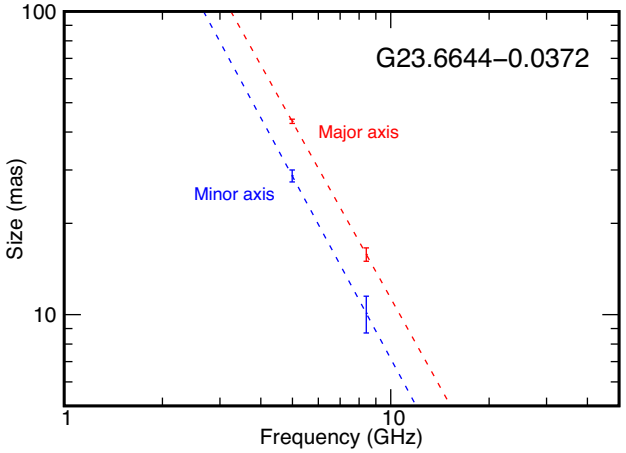

Figure 10. The best-fitting major and minor sizes of G23.6644–0.0372 and their strong dependence on the observing frequency. The dashed lines represent the power-law models: $\theta(\nu) = 970.5\nu^{-1.93}$ (red) and $\theta(\nu) = 712.4\nu^{-2.00}$ (blue).

scattering disc with major by minor axes of 34 by 19 mas at 5 GHz (Kounkel et al. 2018).

G23.6644–0.0372 suffers strong scattering because of its low Galactic latitude (e.g. Cordes et al. 1991; Cordes & Lazio 2003; Pushkarev & Kovalev 2015). For Galactic pulsars, there is a positive correlation between SM and dispersion measure (DM). The DM is defined as

$$\mathrm{DM} = \int_0^D n_e \mathrm{d}s, \tag{10}$$

where n_e is the number density of free electrons. The correlation gives SM ∝ DM^3 for DM > 20 pc cm^{-3} (e.g. Cordes & Lazio 2003). According to the correlation relation, it requires DM $\gtrsim$ 1000 pc cm^{-3} for SM $\gtrsim$ 10 kpc m$^{-20/3}$. In the field of our target, there is a normal radio pulsar J1834–0812: RA = 18$^{\rm h}$34$^{\rm m}$29$^{\rm s}$.8(9), Dec. = −08°12′00(100), period 0.491 s (Bates et al. 2011). The pulsar has a very high DM, 1020 ± 50 cm^{-3} pc, a DM distance of 9.6 ± 1.2 kpc, an average flux density of 0.10 ± 0.02 mJy at 6.5 GHz and a spectral index of −0.7 ± 0.3 between 1.4 and 6.5 GHz (Bates et al. 2011). Within a circle with a centre at G23.6644–0.0372 and a radius of 5°, the pulsar has the highest DM in the ATNF pulsar catalogue.[5] The source G23.6644–0.0372 is within the large 3σ error ellipse (semimajor and semiminor axes: 400 by 300 arcsec) of PSR J1834–0812. However, G23.6644–0.0372 has a rising radio spectrum at frequencies ≤5 GHz(cf. Fig. 11 and discussion below). This spectrum cannot allow us to explain G23.6644–0.0372 as an optically thin pulsar nebula associated with PSR J1834–0812.

The non-simultaneous radio spectrum of G23.6644–0.0372 is displayed in Fig. 11. The red point marks the earliest flux density measurement observed at 5.0 GHz in 1989 (Becker et al. 2010). The blue points represent the flux densities observed between 2001 and 2019. The error bar is at the level 1σ. The arrows represent the upper limits. These flux density data are also listed in Table 7. The non-simultaneous radio spectrum between 2001 and 2019 looks relatively smooth. The non-simultaneous spectral index between 1.4 and 5.0 GHz is ∼2.0. This is a very sharp increase and consistent with the non-detections at <1.4 GHz. The radio spectrum observed at ≥5 GHz between 2005 and 2017 follows the rising tendency,

[5] https://www.atnf.csiro.au/research/pulsar/psrcat/

Downloaded from https://academic.oup.com/mnras/article/511/1/280/6496041 by Chalmers Tekniska Hogskola user on 07 April 2022

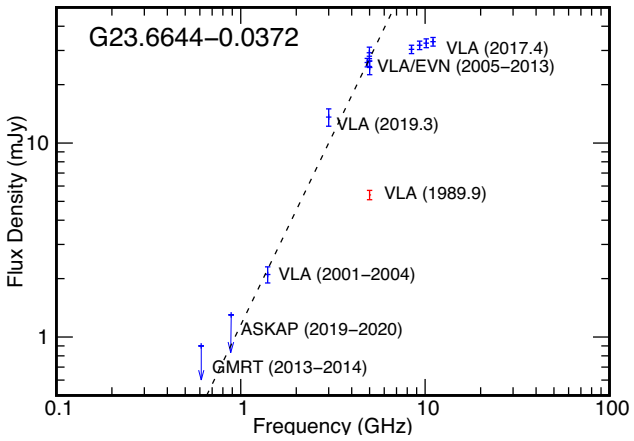

Figure 11. The rising radio spectrum of the variable radio source G23.6644–0.0372. The data are from various non-simultaneous observations and listed in Table 7. The dashed line represents the best-fitting power-law function $S(\nu) = (1.15 \pm 0.21)\nu^{1.97 \pm 0.12}$ derived from the blue points between 1.4 and 5.0 GHz.

Table 7. Summary of the flux densities of G23.6644–0.0372.

Freq. (GHz)	Flux density (mJy)	Array and date (reference)
0.61	$\leq$0.9	GMRT, 2013–2014 (Kijak et al. 2017)
0.89	$\leq$1.3	ASKAP, 2019–2020 (McConnell et al. 2020)
1.40	2.1 $\pm$ 0.2	VLA, 2001–2004 (Becker et al. 2010)
3.00	13.6 $\pm$ 1.4	VLA in 2019 (Lacy et al. 2020)
5.00	5.4 $\pm$ 0.3	VLA in 1989 (Becker et al. 2010)
4.86	26.0 $\pm$ 1.3	VLA in 2005 (Becker et al. 2010)
5.00	23.8 $\pm$ 1.3	WSRT on 2010 Dec 15
5.00	24.5 $\pm$ 2.0	EVN on 2010 Dec 15
4.99	29.2 $\pm$ 2.0	EVN on 2012 Feb 08
4.99	26.4 $\pm$ 1.6	EVN on 2012 Sep 17
8.44	30.4 $\pm$ 1.5	VLA on 2017 June 2
9.34	31.9 $\pm$ 1.6	VLA on 2017 June 2
10.14	32.7 $\pm$ 1.7	VLA on 2017 June 2
11.04	33.3 $\pm$ 1.7	VLA on 2017 June 2

while starts to flatten significantly. It shows a flat spectrum with $\alpha = 0.34 \pm 0.04$ between 8 and 12 GHz.

G23.6644–0.0372 is an intrinsically compact source with an angular size of $\theta_{\rm int} \ll \theta_{\rm maj}$. If we use 10 mas ($0.25\theta_{\rm maj}$ at 5 GHz) as the upper limit for $\theta_{\rm int}$, its intrinsic brightness temperature is expected be at least one order of magnitude higher than the observed value, $(1.1 \pm 0.1) \times 10^6$ K at 5 GHz. Because of the high intrinsic brightness temperature $\geq 10^7$ K, we identify it as a non-thermal radio source. Among all kinds of Galactic non-thermal radio sources, we cannot interpret G23.6644–0.0372 as a pulsar wind nebula, a supernova remnant (e.g. Weiler et al. 2002) or a wind collision region (e.g. Apep, Marcote et al. 2021) in a binary. These Galactic sources usually have counterparts known from multiwavelength observations and show a relatively extended morphology with an optically thin radio spectrum. The object G23.6644–0.0372 is intrinsically compact and relatively bright. Its radio spectrum is optically thick at $\leq$5 GHz and flat between 8.4 and 11.0 GHz. Based on the spectrum of the source and its relatively high flux densities observed at $\geq$5 GHz for more than three decades, we cannot identify G23.6644–0.0372 as a radio pulsar (e.g. Zhao et al. 2020), a magnetar (e.g. Kaspi & Beloborodov 2017), or a stellar-mass black hole in an X-ray binary system (e.g. Pietka et al. 2015). Moreover, there are no X-ray, optical, and infrared counterparts found by Becker et al. (2010) and by us in the latest catalogues of VizieR[6] (Ochsenbein, Bauer & Marcout 2000) and the online multiband images provided by the CORNISH survey (Hoare et al. 2012).

G23.6644–0.0372 is most likely an extragalactic source with a peaked radio spectrum. The rising radio spectrum of G23.6644–0.0372 in Fig. 11 is frequently seen in AGN (cf. a review by O'Dea & Saikia 2021). As a non-thermal radio source, G23.6644–0.0372 is expected to have an optically thin radio spectrum at frequencies $>$11 GHz, and thus can be classified as a high-frequency peaked-spectrum source (e.g. Orienti et al. 2006; O'Dea & Saikia 2021). Between the intrinsic peak frequency $\nu_{\rm pk}$ and the maximum linear size $l_{\rm max}$, this class of sources tend to follow a correlation, $\nu_{\rm pk} \propto l_{\rm max}^{-0.65}$ (O'Dea 1998). According to the correlation, G23.6644–0.0372 would have a linear size of $\lesssim$10 pc.

We favour an intrinsic origin for its flux density variability. At 5 GHz, the source displayed a factor of five increase of the flux density between 1990 and 2005, and then entered a relatively stable phase between 2005 and 2017. The early brightening could be driven by a sudden change of the accretion rate, a newborn jet or a change of the jet direction (e.g. the extreme case NGC 660 Argo et al. 2015). Generally, such large variability on time-scales of decades is inconsistent with an extrinsic variability on short time-scales of $\lesssim$1 yr due to plasma propagation effects (e.g. Nyland et al. 2020). Similar extragalactic variable radio sources with the convex radio spectra peaking at $\gtrsim$3 GHz have been reported by Orienti & Dallacasa (2020) and Wołowska et al. (2021). Their optical counterparts are most likely quasars. VLBI observations of these radio sources often reveal compact structures on the parsec scales (e.g. Orienti & Dallacasa 2020; Wołowska et al. 2021). Their multiband radio spectra also show significant variation. Some sources flattened their spectra and changed their flux densities more randomly, indicating they are significantly beamed sources and similar to blazars (e.g. Wołowska et al. 2021). Future multi-epoch high-frequency VLBI observations would provide key clues for us to answer whether G23.6644–0.0372 is a beamed source and have a relativistic ejecta. Moreover, the multifrequency monitoring of its radio spectrum also allows us to investigate whether it follows the adiabatic expansion (e.g. Orienti & Dallacasa 2020).

4.2 Contribution from the angular broadening by scattering

All sources in the Galactic plane suffer scatter broadening to some degree. A model of electron distribution in the Galaxy presented by Cordes et al. (1991) offered a prediction of the scatter broadening in the absence of strong clumps of turbulence (see Fig. 3 in the cited paper, $\theta_{\rm scat}$ is 125–1000 mas at 1 GHz). Scaling this prediction to our observing frequency of 5 GHz, we estimate the scattering diameter $\theta_{\rm scat}$ at 5 GHz in the sky areas of our interest being in the range 5–40 mas. Our calibrator J1846–0651 (Galactic latitude: 0.87 deg) has an angular size of 5.03 $\pm$ 0.02 mas. Because of the very low Galactic latitude, G23.6644–0.0372 suffer from the stronger angular broadening (Cordes et al. 1991) in the sample and thus have much larger angular sizes (25–45 mas). Our results are generally consistent with the model predictions. We also notice that the scatter broadening might be very sky position dependent (e.g. Cordes & Lazio 2002, 2003) and there are very limited input pulsar data at the distance of $\gtrsim$5 kpc to constrain electron distribution models (e.g. Yao,

[6] http://vizier.u-strasbg.fr/index.gml

Downloaded from https://academic.oup.com/mnras/article/511/1/280/6496041 by Chalmers Tekniska Hogskola user on 07 April 2022

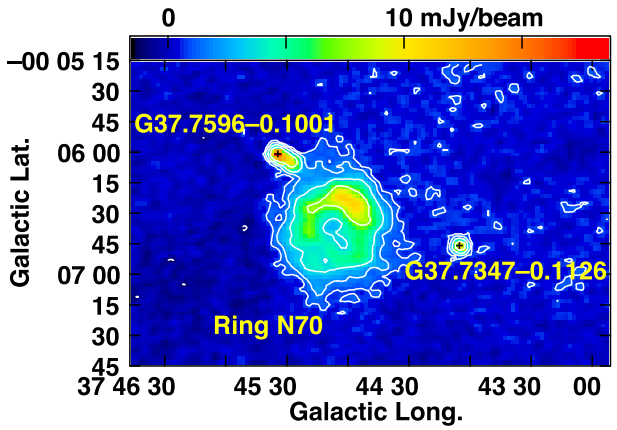

Figure 12. The 1.4-GHz VLA image of the radio source G37.7596–0.1001 and the young H II region G37.7347–0.1126. It is clearly seen that G37.7596–0.1001 shows a 12.5-arcsec-long extension towards south. The image is from the survey MAGPIS (Helfand et al. 2006). The ring structure N70 (Churchwell et al. 2006) is also associated with a Galactic H II region, G37.754–0.108 (White et al. 2005). The sizes of the beam are FWHM = 6.4 × 5.4 arcsec. The map has a peak brightness of 18.5 mJy beam^{-1} and a noise level of σ = 0.36 mJy beam^{-1}. The contours represent the levels 2.5σ × (−1, 1, 2, 4, 8).

Manchester & Wang 2017). The available AGN size measurements are also very rare in particular at the very low Galactic latitude (e.g. Cordes & Lazio 2003; Pushkarev & Kovalev 2015). Thus, the model-estimated $\theta_{\rm scat}$ has a very large uncertainty (up to ∼1 dex). Our constraint $\theta_{\rm FWHM}$ in Table 3 might include a strong contribution from $\theta_{\rm scat}$. There might be more sources intrinsically compact on the centi-arcsec scales.

Several sources might be slightly resolved on the arcsec scales. In Table 3, six sources (No. 2, 5, 10, 12, 15, and 17) have a size ($\theta_{\rm VLAS}$) larger than the beam size (1.5 arcsec) at the level >2σ in the CORNISH images (Hoare et al. 2012; Purcell et al. 2013). Their angular sizes may not be explained as a consequence of extreme strong scatter broadening, $\theta_{\rm scat}$ = 0.34 arcsec at 5 GHz (Moran et al. 1990). Moreover, two sources show a clearly seen extension. The related VLA survey images are displayed in Figs 12 and 13. They also show relatively steep radio spectra in Fig. 14.

4.3 Classifications of the 17 variable sources

Three sources can be firmly identified as Galactic objects in our sample. These Galactic objects have clearly seen infrared counterparts in the online multiwavelength image data base collected by the survey CORNISH (Hoare et al. 2012; Purcell et al. 2013).

Two arcsec-scale extended sources G25.7156+0.0488 and G37.7347–0.1126 are young H II regions (Becker et al. 2010; de la Fuente et al. 2020; Yang et al. 2021c). In Table 5, the two thermal sources, powered by free–free radiation, have flux densities >10 mJy at 1.06 GHz, while drops to <1.3 mJy at frequency 0.88 GHz. This sharp change is mainly because of free–free absorption (de la Fuente et al. 2020; Yang et al. 2021b).

The source G24.5343–0.1020 was identified as a candidate radio star in the CORNISH catalogue (Hoare et al. 2012; Purcell et al. 2013). Marocco et al. (2021) used a programme CATWISE to catalogue sources that are selected from all-sky survey data of *Wide-field Infrared Survey Explorer* (*WISE*) at 3.4 and 4.6 μm, and detected a proper motion, $\mu_{\rm ra}$ = −50.75 ± 5.5 mas yr^{-1}, $\mu_{\rm dec.}$ = −48.9 ± 9.0 mas yr^{-1}, for the source. This input allows us to confirm G24.5343–0.1020 as a radio star. The radio star had a quite large variability. It had a peak brightness of ≤0.9 mJy at 5 GHz in 1990, while brightened significantly and reached 6.8 ± 0.3 mJy in 2006 (Becker et al. 2010) and 8.5 ± 0.7 mJy in 2011. Its non-simultaneous radio spectrum is displayed in Fig. 15. It shows an inverted radio spectrum. If the radio spectrum is because of the significant absorption at the lower frequencies, future radio observations would reveal a flat spectrum for a thermal source or a steep spectrum for a non-thermal source at the frequencies >12 GHz.

The source G25.2048+0.1251 is very likely a compact planetary nebula according to its infrared and radio properties. Its non-simultaneous radio spectrum is displayed in Fig. 16. This is a frequently seen radio spectrum in planetary nebulae (e.g. Irabor et al. 2018). Because of significant variability or absorption at the low frequencies, its radio spectrum cannot be accurately described by a simple power-law model. It has a faint infrared counterpart. In the Spitzer Galactic Legacy Infrared Mid-Plane Survey Extraordinaire (GLIMPSE), it has an increasing flux density from ∼1.4 mJy at 3.6 μm to ∼19.4 mJy at 8.0 μm (Benjamin et al. 2003; Churchwell et al. 2009). It is also detected by the *WISE* at 24 μm and shows a compact morphology (≲1 arcsec) with a flux density of ∼9.2 mJy. Most likely, its spectral energy distribution peaks at ≲24 μm, strongly supporting the classification of a planetary nebula instead of a young H II region (Irabor et al. 2018). Moreover, some planetary nebulae are known to show large radio variability probably resulting from non-thermal radio emission mechanism (e.g. Cerrigone et al. 2017). However, the VLBI non-detection at 5 GHz does not support the existence of non-thermal emission of $T_{\rm b} \geq 2 \times 10^5$ K. If it is indeed a planetary nebula, its nearly flat spectrum indicates that the dominant radio continuum emission is thermal emission at ≳5 GHz.

The above candidate planetary nebula G025.2048+0.1251 plus the other 13 sources are listed as candidate radio AGN in the CORNISH catalogue (Hoare et al. 2012; Purcell et al. 2013) mainly because of no clearly seen counterparts in the optical and infrared wavelengths. We also searched for multiwavelength counterparts in the catalogues of VizieR, and possible associated astrophysical masers in the online maser data base [7] presented by Ladeyschikov, Bayandina & Sobolev (2019) from the available literature and private catalogues. Except for G25.2048+0.1251, we did not find any counterparts or associated masers in these catalogues and online multiband image data bases. For a Galactic source with an angular size in our observed range (≲2000 mas) at a typical distance of 10 kpc, it will have a physical size of ≲0.1 pc and thus can vary rapidly on time-scales of ≲0.3 yr (e.g. Zhao et al. 2020). However, nine sources did not vary significantly over a 4-yr time-scale (cf. Table 3). Thus, the explanation of the extragalactic radio AGN are also more consistent with our results.

The spectral indices of the 17 sources in Table 5 are also displayed in Fig. 14. According to the non-simultaneous spectral indices observed by the ASKAP and the VLA over a time-scale of about 1 yr and assuming no significant (>15 per cent) variability, these sources can be clearly divided into two classes. Seven sources have rising spectra with spectral indices $\alpha > 1$ between 0.88 and 3.00 GHz. This class of sources includes three Galactic objects, a candidate planetary nebula, and the most compact source G23.6644–0.0372 (cf. the VLBI image in Fig. 6). The remaining 10 sources have flat or steep spectra with spectral indices $\alpha \lesssim 0$. Together with the simultaneous spectral indices between 1 and 2 GHz provided by Bihr et al. (2016), we notice that two sources (G22.9116–0.2878/No. 2 in

[7] http://maserdb.net/

Downloaded from https://academic.oup.com/mnras/article/511/1/280/6496041 by Chalmers Tekniska Hogskola user on 07 April 2022

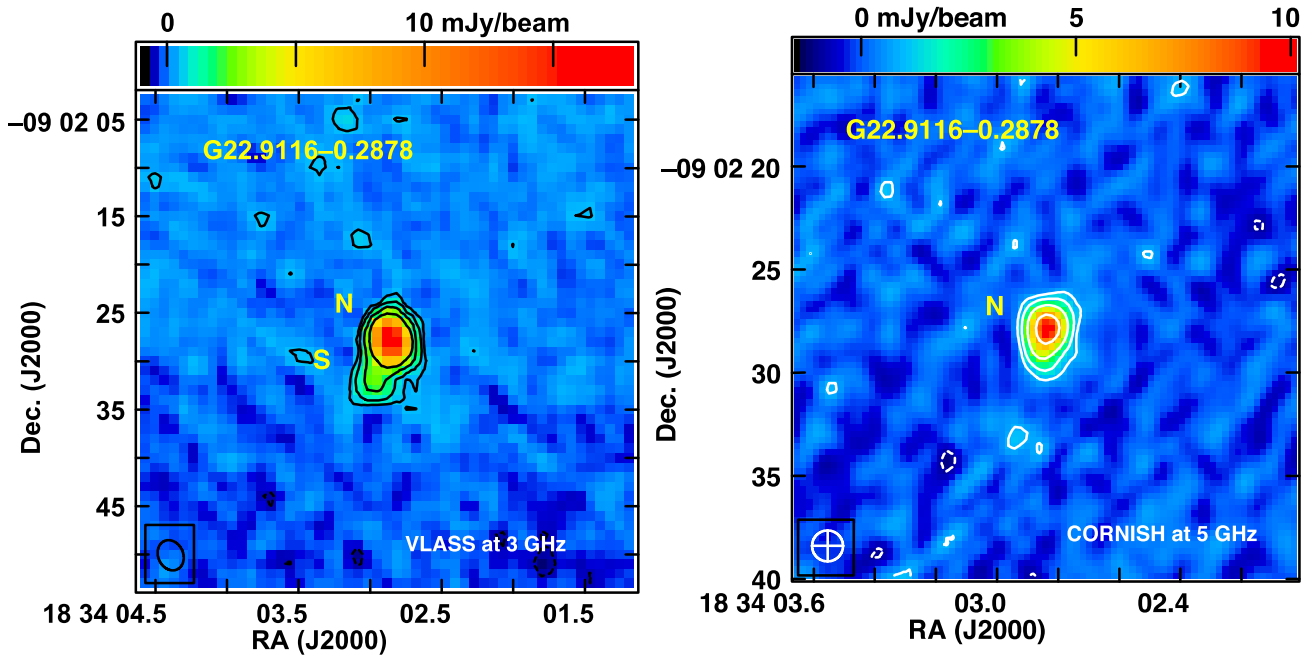

Figure 13. The arcsec-scale structure of the steep-spectrum source G22.9116–0.1939 observed by the VLA surveys VLASS (Lacy et al. 2020) and CORNISH (Hoare et al. 2012; Purcell et al. 2013). The contours represent the levels $2.5\sigma \times (-1, 1, 2, 4, 8)$. The 3-GHz map has a peak brightness of 17.8 mJy beam^{-1} and an off-source noise level of $\sigma = 0.2$ mJy beam^{-1}. The 5-GHz map has a peak brightness of 10.0 mJy beam^{-1} and a noise level of $\sigma = 0.35$ mJy beam^{-1}. The beam FWHM is 3.3 × 2.2 arcsec at 3 GHz and 1.5 × 1.5 arcsec at 5 GHz. The integrated flux density is 28.7 ± 1.4 mJy at 3 GHz and 15.5 ± 1.6 mJy at 5 GHz.

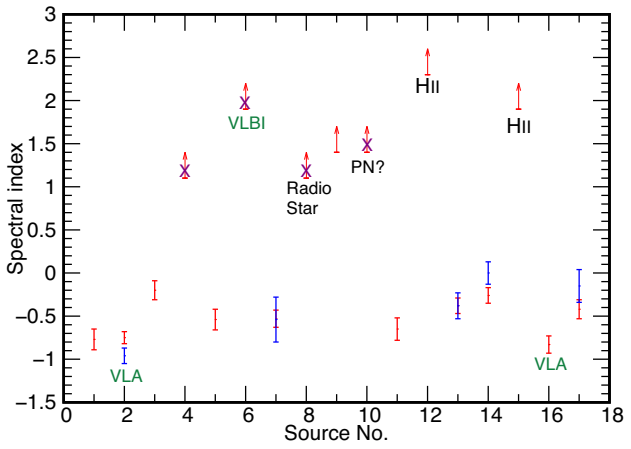

Figure 14. The spectral indices and the diverse nature of the sample. Red points represent the spectral indices between 0.88 and 3.00 GHz. Red arrows represent the lower limits. Blue points represent the spectral indices between 1.00 and 2.00 GHz. The error bars are at the level of 1σ. The input data are listed in Table 5. Purple crosses show the sources observed by the Jansky VLA at *X* band and listed in Table 4. The notes in black highlight three Galactic sources and one candidate planetary nebula (PN). The notes in green indicate the sources displaying the significantly extended structures in the VLBI (cf. Fig. 6) and VLA images (cf. Figs 12 and 13).

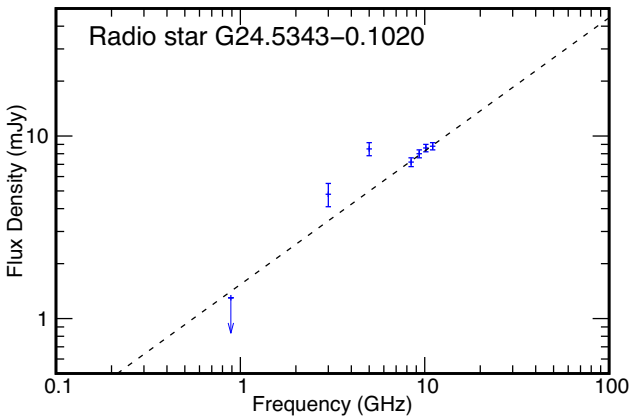

Figure 15. The rising radio spectra of the variable radio star G24.5343–0.1020. The data are from various non-simultaneous observations between 2011 and 2020 and listed in Tables 3–5. The dashed line represents the best-fitting model $S(\nu) = (1.53 \pm 0.48)\nu^{0.73 \pm 0.14}$ derived from the data points at frequencies > 8 GHz.

Fig. 13 and G37.7596–0.1101/No. 16 in Fig. 12) have steep spectra with $\alpha < -0.5$ and one source (G26.2818+0.2312/No. 14) has a flat spectrum with $|\alpha| < 0.5$.

According to the observed structures and radio spectra, three sources are very likely AGN jets. The source G23.6644–0.0372 has been discussed in detail in Section 4.1. Furthermore, the steep-spectrum source G37.7596–0.1001 shows an elongated morphology at 1.4 GHz with a de-convolved length of ∼12.5 arcsec in the survey MAGPIS (Helfand et al. 2006). The structure is also shown in Fig. 12. In the images provided by the CORNISH at 5 GHz (Hoare et al. 2012; Purcell et al. 2013) and the VLASS at 3 GHz (Lacy et al. 2020), the other steep-spectrum source G22.9116–0.2878 shows a 4.5-arcsec extension towards south. This extension is also displayed in Fig. 13. The faint extensions are not clearly seen in the 5-GHz CORNISH images probably because of their steep spectra. Together with their linear structure, we explain these faint arcsec-scale extensions as the collimated jet activity.

Downloaded from https://academic.oup.com/mnras/article/511/1/280/6496041 by Chalmers Tekniska Hogskola user on 07 April 2022

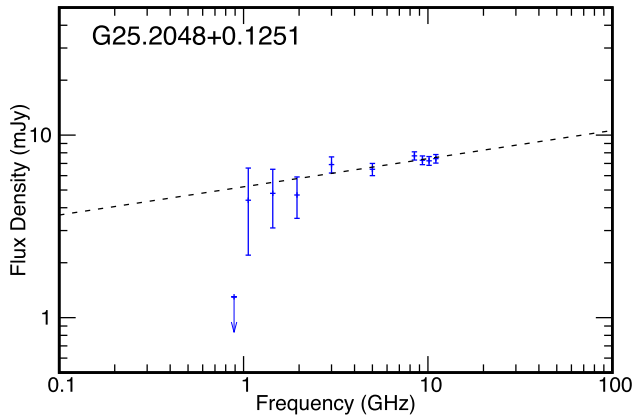

Figure 16. The rising radio spectra of the variable source G25.2048+0.1251. The data are from various non-simultaneous observations between 2011 and 2020 and listed in Tables 3–5. The dashed lines represent the best-fitting model $S(\nu) = (5.2 \pm 0.5)\nu^{0.15 \pm 0.05}$ derived from the data points at frequencies > 1 GHz.

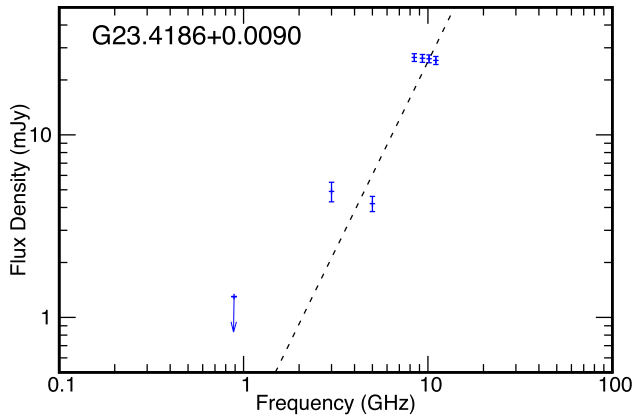

Figure 17. The rising radio spectra of the variable source G23.4186+0.0090. The data are from various non-simultaneous observations between 2011 and 2020 and listed in Tables 3–5. The dashed lines represent the best-fitting model $S(\nu) = (0.22 \pm 0.23)\nu^{2.05 \pm 0.48}$ derived from the data points at frequencies > 1 GHz.

In the remaining 11 candidate radio AGN, three sources (No. 4, 9, and 10) have rising radio spectra. They have a peak frequency $\gtrsim$3 GHz. Their non-simultaneous radio spectra are displayed in Figs 16, 17, and 18. For each source, we tried to fit its spectrum to a simple power-law function. Because of spectral variability and possible absorption at <1 GHz, the model, i.e. the dashed line, gives a relatively poor description to the data. They are likely intrinsically compact radio AGN with the convex radio spectra (O'Dea & Saikia 2021). Using the correlation of $\nu_{\rm pk} \propto l_{\rm max}^{-0.65}$ (O'Dea 1998), they would have a linear size of $\lesssim$100 pc. Their radio spectra might vary significantly and become flat at a certain time (e.g. Orienti & Dallacasa 2020). Their optical counterparts are likely quasars instead of galaxies (e.g. Wołowska et al. 2021).

The other eight sources have flat or steep spectra. Compared to the peak $\alpha = -0.71$ of the spectral index distribution found by Gordon et al. (2021) in about half million radio sources between 1.4 and 3.0 GHz, these sources have relatively flatter spectra. Together with their compact morphology in the CORNISH images and their variability on decadal time-scales, they would represent relatively

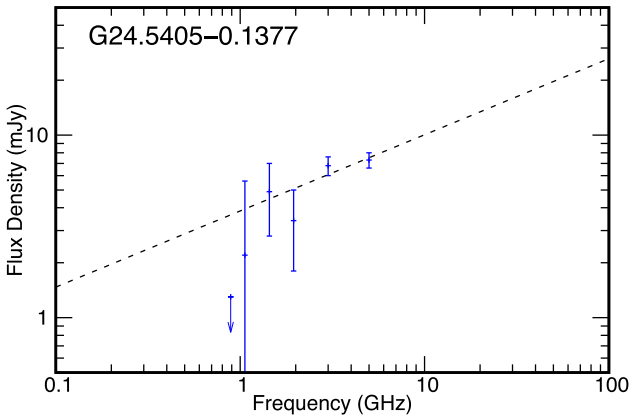

Figure 18. The rising radio spectra of the variable source G24.5405–0.1377. The data are from various non-simultaneous observations between 2011 and 2020 and listed in Tables 3 and 5. The dashed lines represent the best-fitting model $S(\nu) = (3.84 \pm 0.41)\nu^{0.42 \pm 0.18}$ derived from the data points at frequencies > 1 GHz.

young and compact radio AGN activity (e.g. O'Dea & Saikia 2021). Some sources might be young or new-born jets on the pc scales if they have inverted radio spectra peaking at frequencies <0.9 GHz (e.g. Ross et al. 2021). The sources G26.0526–0.2426, G22.9743–0.3920, G26.2818+0.2312, and G39.1105–0.0160 might also be faint blazars with flat-spectrum and variable radio cores (e.g. Ciaramella et al. 2004; Cheng et al. 2020). We cannot fully exclude the possibility of being bright non-thermal slow transients in their host galaxies, such as the decades-long transient FIRST J141918.9+394036 (Law et al. 2018). However, this kind of possibility is very low for the small sky area ∼10 deg^2 (e.g. Murphy et al. 2021). Furthermore, all the sources were still significantly detected in the VLASS at 3.0 GHz over about three decades since the early VLA 5-GHz Galactic plane survey between 1989 and 1991 (Becker et al. 1994, 2010). Their kpc-scale host galaxies and jets might show similar spectra (e.g. Zajaček et al. 2019) and contribute a certain diffuse radio emission to the total radio flux densities (Linden et al. 2020), while their contributions are expected to be very stable on decadal time-scales. Thus, we cannot associate their radio variability to their kpc-scale host galaxies or diffuse jets. Because none of these sources has an arcsec-scale extended radio lobe and a bright centi-arcsec-scale feature, we cannot explain the variability as a consequence of some hotspots in the extended lobes.

Three sources G23.5585–0.3241, G37.7347–0.1126 (H II region), and G37.7596–0.1001 were not detected by Becker et al. (2010) in the first epoch 1990+. They also cannot be identified as one-off astrophysical transients because these non-detections at 5 GHz are questionable according to the multifrequency and multi-epoch online VLA images[8] provided by the MAGPIS (Helfand et al. 2006). The source G23.5585–0.3241 was detected with a peak brightness of 0.75 ± 0.15 mJy beam^{-1} in the first epoch 1990+. The two sources G37.7347–0.1126 and G37.7596–0.1001 are located in a very crowded field (cf. the 1.4-GHz VLA image, Fig. 12). The online 5-GHz VLA image of the two sources in the first epoch 1990+ has a poor quality and shows some strong image artefacts most likely resulting from a poor de-convolution of the complex field. Furthermore, G37.7596–0.1001 was detected with a peak brightness of 11.8 ± 1.8 mJy beam^{-1} at 1.4 GHz in 1983 (Becker et al. 1990).

[8]https://third.ucllnl.org/cgi-bin/gpscutout

Downloaded from https://academic.oup.com/mnras/article/511/1/280/6496041 by Chalmers Tekniska Hogskola user on 07 April 2022

According to the above discussion, we give some comments in Table 3. Our analyse shows that the sample has a divers nature. Among these variable sources of $\gtrsim$1 mJy in the Galactic plane, AGN activity still plays a dominant role. We caution that there might still exist faint centi-arcsec-scale compact components that were missed in a certain sources because of their variability and our limited baseline sensitivity. Future multifrequency radio observations of the sample with the electronic Multi-Element Remotely Linked Interferometer Network would have ideal resolutions to further reveal their structures and probe their natures.

5 CONCLUSIONS

With the EVN at 5 GHz, we observed 17 variable sources with a Galactic latitude $<1^\circ$. We detected only G23.6644–0.0372 in the high-resolution VLBI images, yet all the sources in the low-resolution WSRT images. Moreover, we performed another two-epoch EVN observations of the detected source G23.6644–0.0372. It had a stable flux density of 26.8 ± 1.8 mJy between 2010 December and 2012 September. Its radio structure is fully in agreement with an elliptical Gaussian model with the angular sizes 43.4 ± 0.7 mas by 28.7 ± 1.3 mas at position angle $39\overset{\circ}{.}4 \pm 2\overset{\circ}{.}7$. Together with its inverted radio spectrum and long-term flux density variability, the structure could be interpreted as a compact extragalactic source plus a strong scatter broadening. We noticed two young H II regions that were previously classified in literature, and identified a radio star and a candidate planetary nebula. Furthermore, we studied the spectral properties of the rest of the candidate radio AGN that have no optical and infrared counterparts. Using the non-simultaneous flux density measurements observed by the RACS at 0.9 GHz and the VLASS at 3.0 GHz with an interval of about 1 yr, we found that three sources have rising spectra and the remaining 10 sources have flat or steep spectra with $\alpha > -1$. In the existing VLA survey images, two sources display faint jet activity on the arcsec scales. Our study indicates that the sample has a diverse nature and AGN activity plays a dominant role among variable sources of $\gtrsim$1 mJy in the Galactic plane.

ACKNOWLEDGEMENTS

The authors are grateful to James Miller-Jones, Pikky Atri, and Arash Bahramian for a very useful discussion and permission to compare results presented here with the complementary VLBA observations before publication of the latter. This work is supported by the National Science Foundation of China (grants 11763002, 11590784, 11933007) and the National SKA Program of China No. 2020SKA0110100. The EVN is a joint facility of independent European, African, Asian, and North American radio astronomy institutes. Scientific results from data presented in this publication are derived from the following EVN project code(s): EY014 and EY017. e-VLBI research infrastructure in Europe is supported by the European Union's Seventh Framework Programme (FP7/2007-2013) under grant agreement number RI-261525 NEXPReS. The research leading to these results has received funding from the European Commission Seventh Framework Programme (FP/2007-2013) under grant agreement number 283393 (RadioNet3). The VLA is operated by the NRAO, which is a facility of the National Science Foundation operated under cooperative agreement by Associated Universities, Inc. This research has used NASA's Astrophysics Data System Bibliographic Services and the NASA/IPAC Extragalactic Database (NED), which is operated by the Jet Propulsion Laboratory, California Institute of Technology, under contract with the National Aeronautics and Space Administration, the VizieR catalogue access tool, CDS, Strasbourg, France (DOI: 10.26093/cds/vizier). This research has made use of the CIRADA cutout service at URL cutouts.cirada.ca, operated by the Canadian Initiative for Radio Astronomy Data Analysis (CIRADA). CIRADA is funded by a grant from the Canada Foundation for Innovation 2017 Innovation Fund (Project 35999), as well as by the Provinces of Ontario, British Columbia, Alberta, Manitoba, and Quebec, in collaboration with the National Research Council of Canada, the US NRAO and Australia's Commonwealth Scientific and Industrial Research Organization.

DATA AVAILABILITY

The correlation data of the experiments EY014, EY017A, and EY017B are available in the EVN data archive (http://www.jive.nl/select-experiment). The calibrated visibility data underlying this article will be shared on reasonable request to the corresponding author. The VLA data are available in the NRAO Science Data Archive (https://archive.nrao.edu/archive/advquery.jsp. The WSRT data are available in the WSRT archive (https://old.astron.nl/radio-observatory/astronomers/wsrt-archive).

REFERENCES

Aguirre J. E. et al., 2011, ApJS, 192, 4
Argo M. K., van Bemmel I. M., Connolly S. D., Beswick R. J., 2015, MNRAS, 452, 1081
Atri P. et al., 2020, MNRAS, 493, L81
Bates S. D. et al., 2011, MNRAS, 411, 1575
Beasley A. J., Conway J. E., 1995, in Zensus J. A., Diamond P. J., Napier P. J., eds, ASP Conf. Ser. Vol. 82, Very Long Baseline Interferometry and the VLBA. Astron. Soc. Pac., San Francisco, p. 327
Becker R. H., White R. L., McLean B. J., Helfand D. J., Zoonematkermani S., 1990, ApJ, 358, 485
Becker R. H., White R. L., Helfand D. J., Zoonematkermani S., 1994, ApJS, 91, 347
Becker R. H., Helfand D. J., White R. L., Proctor D. D., 2010, AJ, 140, 157
Benjamin R. A. et al., 2003, PASP, 115, 953
Bihr S. et al., 2016, A&A, 588, A97
Brunthaler A. et al., 2021, A&A, 651, A85
Carey S. J. et al., 2009, PASP, 121, 76
Cerrigone L., Umana G., Trigilio C., Leto P., Buemi C. S., Ingallinera A., 2017, MNRAS, 468, 3450
Charlot P. et al., 2020, A&A, 644, A159
Cheng X. P. et al., 2020, ApJS, 247, 57
Chomiuk L. et al., 2014, Nature, 514, 339
Churchwell E. et al., 2006, ApJ, 649, 759
Churchwell E. et al., 2009, PASP, 121, 213
Ciaramella A. et al., 2004, A&A, 419, 485
Condon J. J., Condon M. A., Gisler G., Puschell J. J., 1982, ApJ, 252, 102
Cordes J. M., Lazio T. J. W., 2002, preprint(astro-ph/0207156)
Cordes J. M., Lazio T. J. W., 2003, preprint(astro-ph/0301598)
Cordes J. M., Weisberg J. M., Frail D. A., Spangler S. R., Ryan M., 1991, Nature, 354, 121
de la Fuente E., Porras A., Trinidad M. A., Kurtz S. E., Kemp S. N., Tafoya D., Franco J., Rodríguez-Rico C., 2020, MNRAS, 492, 895
de Vries W. H., Becker R. H., White R. L., Helfand D. J., 2004, AJ, 127, 2565
Ding H. et al., 2020, MNRAS, 498, 3736
Dong D. et al., 2021, Science, 373, 1125
Fey A. L., Spangler S. R., Cordes J. M., 1991, ApJ, 372, 132
Gordon Y. A. et al., 2021, ApJS, 255, 30
Greisen E. W., 2003, in Heck A., ed., Astrophysics and Space Science Library, Vol. 285, Information Handling in Astronomy - Historical Vistas. Kluwer, Dordrecht, p. 109
Güdel M., 2002, ARA&A, 40, 217
Hands A. D. P., Warwick R. S., Watson M. G., Helfand D. J., 2004, MNRAS, 351, 31

Downloaded from https://academic.oup.com/mnras/article/511/1/280/6496041 by Chalmers Tekniska Hogskola user on 07 April 2022

Helfand D. J., Becker R. H., White R. L., Fallon A., Tuttle S., 2006, AJ, 131, 2525
Hoare M. G. et al., 2012, PASP, 124, 939
Hovatta T., Tornikoski M., Lainela M., Lehto H. J., Valtaoja E., Torniainen I., Aller M. F., Aller H. D., 2007, A&A, 469, 899
Immer K. et al., 2011, ApJS, 194, 25
Irabor T. et al., 2018, MNRAS, 480, 2423
Johnson M. D. et al., 2018, ApJ, 865, 104
Kaspi V. M., Beloborodov A. M., 2017, ARA&A, 55, 261
Keimpema A. et al., 2015, Exp. Astron., 39, 259
Kettenis M., van Langevelde H. J., Reynolds C., Cotton B., 2006, in Gabriel C., Arviset C., Ponz D., Enrique S., eds, ASP Conf. Ser. Vol. 351, Astronomical Data Analysis Software and Systems XV. Astron. Soc. Pac., San Francisco, p. 497
Kijak J., Basu R., Lewandowski W., Rożko K., Dembska M., 2017, ApJ, 840, 108
Kounkel M. et al., 2018, AJ, 155, 218
Lacy M. et al., 2020, PASP, 132, 035001
Ladeyschikov D. A., Bayandina O. S., Sobolev A. M., 2019, AJ, 158, 233
Law C. J., Gaensler B. M., Metzger B. D., Ofek E. O., Sironi L., 2018, ApJ, 866, L22
Linden S. T., Murphy E. J., Dong D., Momjian E., Kennicutt R. C. J., Meier D. S., Schinnerer E., Turner J. L., 2020, ApJS, 248, 25
McConnell D. et al., 2020, PASA, 37, e048
McMullin J. P., Waters B., Schiebel D., Young W., Golap K., 2007, in Shaw R. A., Hill F., Bell D. J., eds, ASP Conf. Ser. Vol. 376, Astronomical Data Analysis Software and Systems XVI. Astron. Soc. Pac., San Francisco, p. 127
Marcote B., Callingham J. R., De Becker M., Edwards P. G., Han Y., Schulz R., Stevens J., Tuthill P. G., 2021, MNRAS, 501, 2478
Marocco F. et al., 2021, ApJS, 253, 8
Mooley K. P. et al., 2016, ApJ, 818, 105
Moran J. M., Rodriguez L. F., Greene B., Backer D. C., 1990, ApJ, 348, 147
Murphy T. et al., 2021, PASA, 38, e054
Nyland K. et al., 2020, ApJ, 905, 74
O'Dea C. P., 1998, PASP, 110, 493
O'Dea C. P., Saikia D. J., 2021, A&A Rev., 29, 3
Ochsenbein F., Bauer P., Marcout J., 2000, A&AS, 143, 23
Orienti M., Dallacasa D., 2020, MNRAS, 499, 1340
Orienti M., Dallacasa D., Tinti S., Stanghellini C., 2006, A&A, 450, 959
Pearson T. J., 1995, in Zensus J. A., Diamond P. J., Napier P. J., eds, ASP Conf. Ser. Vol. 82, Very Long Baseline Interferometry and the VLBA. Astron. Soc. Pac., San Francisco, p. 267
Perley R. A., Butler B. J., 2017, ApJS, 230, 7
Petrov L., 2021, AJ, 161, 14
Pietka M., Fender R. P., Keane E. F., 2015, MNRAS, 446, 3687
Price S. D., Egan M. P., Carey S. J., Mizuno D. R., Kuchar T. A., 2001, AJ, 121, 2819
Pritchard J. et al., 2021, MNRAS, 502, 5438
Purcell C. R. et al., 2013, ApJS, 205, 1
Pushkarev A. B., Kovalev Y. Y., 2015, MNRAS, 452, 4274
Reid M. J., Honma M., 2014, ARA&A, 52, 339
Rioja M. J., Dodson R., 2020, A&A Rev., 28, 6
Ross K. et al., 2021, MNRAS, 501, 6139
Schilizzi R. T. et al., 2001, Exp. Astron., 12, 49
Shen Z.-Q., Lo K. Y., Liang M. C., Ho P. T. P., Zhao J. H., 2005, Nature, 438, 62
Shepherd M. C., Pearson T. J., Taylor G. B., 1994, BAAS, 26, 987
Sugizaki M., Mitsuda K., Kaneda H., Matsuzaki K., Yamauchi S., Koyama K., 2001, ApJS, 134, 77
Szomoru A., 2008, The Role of VLBI in the Golden Age for Radio Astronomy, Sissa Medialab srl, Bologna, p. 40
Trotter A. S., Moran J. M., Rodríguez L. F., 1998, ApJ, 493, 666
Wang Y. et al., 2018, A&A, 619, A124
Wang Y. et al., 2020, A&A, 641, C1
Wang Z. et al., 2021, ApJ, 920, 45
Weiler K. W., Panagia N., Montes M. J., Sramek R. A., 2002, ARA&A, 40, 387
White R. L., Becker R. H., Helfand D. J., 2005, AJ, 130, 586
Wołowska A. et al., 2021, ApJ, 914, 22
Yang J., Paragi Z., van der Horst A. J., Gurvits L. I., Campbell R. M., Giannios D., An T., Komossa S., 2016, MNRAS, 462, L66
Yang A. Y., Thompson M. A., Tian W. W., Bihr S., Beuther H., Hindson L., 2019, MNRAS, 482, 2681
Yang J., Gurvits L. I., Paragi Z., Frey S., Conway J. E., Liu X., Cui L., 2020, MNRAS, 495, L71
Yang J., Paragi Z., Nardini E., Baan W. A., Fan L., Mohan P., Varenius E., An T., 2021a, MNRAS, 500, 2620
Yang J. et al., 2021b, MNRAS, 502, L61
Yang A. Y. et al., 2021c, A&A, 645, A110
Yao J. M., Manchester R. N., Wang N., 2017, ApJ, 835, 29
Zajaček M. et al., 2019, A&A, 630, A83
Zhao J.-H., Morris M. R., Goss W. M., 2020, ApJ, 905, 173

This paper has been typeset from a TEX/LATEX file prepared by the author.

Downloaded from https://academic.oup.com/mnras/article/511/1/280/6496041 by Chalmers Tekniska Hogskola user on 07 April 2022